ARTICLE IN PRESS

Petrography and geochemistry of the Dales Gorge banded iron formation: Paragenetic sequence, source and implications for palaeo-ocean chemistry

E. Pecoits [a,*], M.K. Gingras [a], M.E. Barley [b], A. Kappler [c], N.R. Posth [c], K.O. Konhauser [a]

[a] Department of Earth and Atmospheric Sciences, University of Alberta, 1-26 Earth Sciences Building, Edmonton, AB, T6G 2E3, Canada
[b] School of Earth and Environment, The University of Western Australia, 35 Stirling Highway, Crawley, WA 6009, Australia
[c] Geomicrobiology Group, Center for Applied Geosciences, University of Tübingen, Sigwartstrasse 10, D-72076 Tübingen, Germany

ARTICLE INFO

ABSTRACT

Banded iron formations (BIFs) have long been considered marine chemical precipitates or, as more recently proposed, the result of episodic density flows. In this study, we examined the mineralogy, petrography and chemistry of the Dales Gorge BIF to evaluate the validity of these models. Microbands reflect a compositionally variable primary precipitation/sedimentation pattern with diagenetic modifications. "Iron-rich" bands are characterized by massive anhedral aggregates and xenomorphic hematite, commonly showing overgrowths of subhedral magnetite with minor apatite and late diagenetic ankerite-Fe dolomite. "Iron-poor" bands consist of fine-grained quartz, siderite and Fe-talc in variable amounts. Amorphous silica, ferrihydrite (precursor of hematite), greenalite and possibly some siderite constitute the primary precipitates, while ankerite-Fe dolomite, Fe-talc and magnetite and the bulk of siderite are secondary mineral phases. Ankerite and Fe-dolomite most likely represent by-products of siderite dissolution and the subsequent reaction of dissolved bicarbonate with Ca, Mg and Fe. Ferroan-talc is thought to be formed from the following reactions: (i) greenalite + chert, and (ii) siderite + chert. Magnetite formed from the conversion of hematite, likely through bacterial Fe(III) reduction. Geochemical mineral analyses show that all the phases have very low concentrations of trace elements with the exception of Ba, As, Cr, Zn and Sr. This partitioning was presumably controlled by both sorptive reactions occurring during primary precipitation in the water column and secondary remobilization during diagenesis. Whole-rock analyses indicate two decoupled sources for BIF and S macrobands. While BIF macrobands have a major hydrothermal influence, data from the S macrobands supports a dominantly mafic provenance. Nonetheless, when all the lithologies (i.e., source rocks, S and BIF macrobands) are evaluated together, continuous geochemical trends can be observed. This suggests that at least part of the precursor material of BIF macrobands was sourced from the same material that gave origin to the S macrobands. Similar relationships are seen in other BIF successions, where the evolution from an ultamafic- to a mafic-dominated upper continental crust is distinctly reflected in BIF compositions through time. Interpretation of this data implies that any model developed to explain BIF deposition must consider: (i) processes involving low-temperature weathering of the continental and ocean basement rocks, mainly (ultra)mafic lithologies; and (ii) high temperature water–rock reactions associated with hydrothermal activity at spreading ridge centers or seamounts. In either case, the influence of the compositional change of the upper continental crust played a major role in the chemical compositions of BIFs through time.

1. Introduction

Banded iron formation (BIF) is a lithological term applied to a chemical sedimentary rock consisting of – in its least metamorphosed state – successive layers of fine-grained quartz, iron oxides, carbonates and silicates (Trendall and Blockley, 1970). Such lithologies are the result of both primary mineralogical properties and diagenetic or metamorphic overprinting (Klein, 2005). Banding is observed on a wide range of scales, from coarse macrobands (meters in thickness) to mesobands (centimeter thick units) to millimeter and sub-millimeter layers (Trendall and Blockley, 1970). Among the latter is the wide variety of varve-like repetitive laminae, known as microbands.

BIFs formed throughout much of the Precambrian (~3800 to 545 Ma), reaching maximum abundance between 2700 and 2300 million years ago. It is precisely this time frame which may have witnessed profound changes in the redox state of the oceans and atmosphere, such as the 'Great Oxidation Event' (Holland, 2006).

* Corresponding author. Tel.: +1 780 492 2571; fax: +1 780 492 2030.
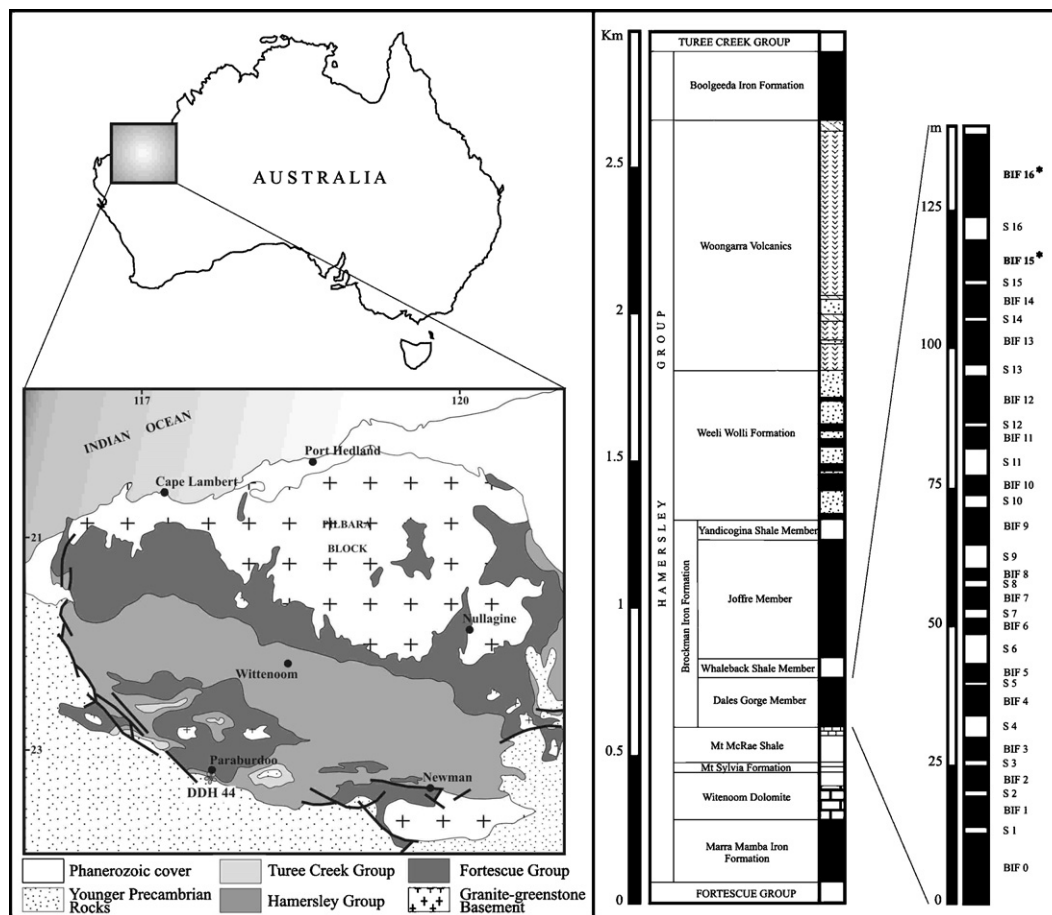E-mail address: epecoits@ualberta.ca (E. Pecoits).

Fig. 1. Regional map and stratigraphic column of the Hamersley Group showing the location of the diamond drillhole DDH-44 and core samples used in this study (modified from Trendall, 1983; Morris, 1993).

The deposition of BIFs have thereby been linked to significant compositional changes in the Earth's atmosphere and hydrosphere, and possibly the diversification of the biosphere (Konhauser et al., 2009). For example, traditional models of BIF deposition propose Fe(II) was oxidized in the presence of free oxygen derived from oxygenic microbial photosynthesis (e.g., James, 1988; Klein and Beukes, 1989; Morris, 1993). Therefore, the link between BIFs and the rise of oxygen in the atmosphere has been a recurrent topic since the early work of Cloud (1965). Other models invoke oxidation of dissolved Fe(II) by anaerobic photosynthetic bacteria, negating the need for the presence of O_2-producing microbes (Konhauser et al., 2002; Kappler et al., 2005; Posth et al., 2008). The decline in BIFs, after about 2300 Ma, has subsequently been attributed to either the rise in bottom water O_2 concentration (e.g., Holland, 1999), or as more recently proposed, an increase in dissolved sulfide (Canfield, 1998), both of which would have effectively removed dissolved Fe(II) from the bulk ocean waters, and thereby limited Fe(II) transport to BIF depocenters. However, the recent recognition that some of the layers in the 2.5 billion year old Dales Gorge Member of Western Australia were derived from episodic density flows (Krapež et al., 2003; Pickard et al., 2004) constitutes a novel avenue for understanding the genesis of these rocks.

In addition to their effect on major elemental cycles (Fe, C, O, S), the deposition of BIFs would have affected the distribution and mobility of both nutritional elements (e.g., P) and trace metals (e.g., V, Mo): in fact, it is reasonable to argue that their concentrations in BIFs provide important clues to ancient seawater composition and the potential primary productivity of the oceans (Bjerrum and Canfield, 2002; Konhauser et al., 2007a, 2009). There-

fore, their concentration and bioavailability should be reflected in the trace element requirements of marine phytoplankton (Saito et al., 2003) and in sediment-trace element chemistry. A number of previous geochemical studies have measured the isotopic composition and the concentration of major, trace and rare earth elements in BIFs (e.g., Baur et al., 1985; Dymek and Klein, 1988; Jacobsen and Pimentel-Klose, 1988; Beukes and Klein, 1990; Beukes et al., 1990; Kaufman et al., 1990; Derry and Jacobsen, 1990; Bau and Möller, 1993; Klein and Beukes, 1989, 1992, 1993; Hamade et al., 2003). Specifically, some contributions have focused on the geochemical origin of the Hamersley BIFs (Alibert and McCulloch, 1993; Barley et al., 1997; Pickard, 2003), the largest (in terms of bulk Fe), most extensive and thickest known of all BIFs (Trendall, 2002). However, very limited information exists regarding the chemistry and mineralogy of the Dales Gorge Member (e.g., Ewers and Morris, 1981), the archetypal BIF from which many BIF models are based (e.g., Ohmoto et al., 2006; Lascelles, 2007). All of these studies have focused on the bulk composition, which makes it difficult to differentiate which elements were associated with the primary precipitates vs. those which were diagenetically remobilized. It is in this regard that we conducted a detailed study of the mineralogy and microstructure of the Dales Gorge BIF with the aim of reconstructing the paragenetic sequence for the depositional and diagenetic history of that BIF. The paragenetic sequence has also provided a framework to interpret the bulk- and microscale geochemical analyses and thus, to relate the elemental distribution to the initial precipitates with the ultimate goal of establishing the controlling factors in the source and distribution of trace elements.

Table 1
Summary of the main petrological and geochemical characteristics of BIF macrobands #15 (core samples DGM-96) and #16 (core samples DGM-36) of the Dales Gorge Member (Brockman Iron Formation) at the Paraburdoo area. The order of minerals (from top to bottom) is based on relative abundance.

Mineral	Habit	Distribution	Chemical formula	Precursor or reaction	Main trace elements (ppm)
Chert	Microcrystalline-anhedral (<15 μm)	Chert- and siderite-rich microbands	SiO_2	Colloidal silica $Si(OH)_4$	–
Hematite	Massive-anhedral and xenomorphic (<100 μm)	Fe-rich (and siderite-rich) microbands	$Fe_2^{3+}O_3$	Ferrihydrite	Ba: 66; Cr: 25; Sr: 22 (Zn, Ni, As, Y, Cu)
Siderite	Anhedral to subhedral (±rims) (0.02–0.075 mm)	Siderite-rich (and chert-rich) microbands	$(Fe,Mg)CO_3$	Authigenic	As: 62; Zn: 25; Cr: 16
Ferroan-talc	Sheaves (0.02–0.09 mm)	Siderite-rich (and chert-rich) microbands	$(Fe,Mg)_3Si_4O_{10}(OH)_2$	Greenalite; Siderite + quartz	As: 48; Zn: 44; Cr: 13
Magnetite	Subhedral overgrowths (0.025–0.075 mm)	Fe-rich microbands	$Fe^{2+}(Fe^{3+})_2O_4$	Hematite + siderite	Ba: 24; Cr: 20; Sr: 10: (Zn, Ni, As, Y, Cu)
Ankerite-Fe dolomite	Anhedral-poikilotopic (0.125–1 mm)	Thickest Fe-rich microbands	$CaMgFe(CO_3)_2$	Siderite (±hmt)	As: 20: (Cr, Zn)
Apatite	Massive-anhedral to subhedral (10–120 μm)	Fe-rich microbands	$Ca_5(PO_4)_3(F,OH)$	Authigenic	–

2. Methodology

2.1. Core location and samples

The Dales Gorge Member is the lowermost unit of the Brockman Iron Formation in the Hamersley Supergroup (Fig. 1). On the basis of SHRIMP U–Pb ages from zircons extracted from tuffaceous bands, Trendall et al. (2004) proposed a depositional age between 2494 and 2464 Ma for the member. As originally defined by Trendall and Blockley (1970), the unit is composed of 33 alternating hematite–magnetite–chert (BIF) and chert–carbonate–silicate (S) "macrobands". Within the decimeter to meter scale macrobands, there are centimeter-sized mesobands and laminated microbands of iron oxides, iron silicates, iron carbonates, and chert, with minor amounts of pyrite and organic carbon.

Studies that have characterized elemental distributions and abundances support the hypothesis that the primary chemical precipitates were homogenously formed across the Dales Gorge Member depositional basin (Trendall and Pepper, 1977; Ewers and Morris, 1981). Yet, differences in mineralogical associations and stable-isotope geochemistry suggest dissimilar metamorphic conditions across the depositional basin, from Paraburdoo to Wittenoom (Becker and Clayton, 1976; Ewers and Morris, 1981; Smith et al., 1982; Baur et al., 1985; Kaufman et al., 1990). More recently, Krapež et al. (2003) and Pickard et al. (2004) suggested that that the S macrobands were derived from episodic density flows, although no evidence of turbidite or clastic deposition have been identified along the 1 m of continuous drill core used for this study.

Two different sets of core samples from Dales Gorge Member (drill hole DDH-44), at Paraburdoo area, were selected from BIF macrobands #15 (samples DGM-96) and #16 (samples DGM-36). The locations of the two sets of samples are shown in Fig. 1. This thick succession is ideally suited for the purpose of this study because of the access to fresh core samples, it has not been significantly metamorphosed (Ewers and Morris, 1981; Kaufman et al., 1990, among others) and it constitutes one of the best-known and largest examples of BIF (Morris, 1993; Trendall, 2002). General descriptions of the various lithofacies are given by Trendall (1983), Krapež et al. (2003) and Pickard et al. (2004) and are not repeated here.

2.2. Analytical techniques

Twenty polished thin sections were prepared and examined using reflected and transmitted light microscopy in order to ascertain the mineralogy, textural relationships and, ultimately, the paragenetic sequence. For bulk trace element analyses, each analysis represents the average composition of a split drill core (1/2″) with a length of about 3–4 cm. Veins and strongly recrystallized zones were avoided to minimize the effects of diagenetic or metamorphic overprinting. Ten core samples were mechanically subdivided into chips without metal contact. Between 20 and 150 g of the material was powdered in an automated agate mill. Crushed rock powders (<100 mesh) were dissolved with $HF + HNO_3$ and analyzed using a PerkinElmer Elan6000 Quad-ICP-MS (quadrupole inductively coupled plasma mass spectrometer). Accuracy and precision of the analytical protocol is verified with the use of well-established international whole-rock standards (Basalt, CRPG Nancy).

Major and minor element analyses (K, Na, Si, Fe, P, Mg, Cl, Al, Mn) of minerals from thin sections were acquired using a JEOL Microprobe 8900. The same instrument was used to produce secondary and backscattered electron images as well as elemental distribution maps. Natural minerals were employed as standards as described in Jarosewich (2002; and references therein). Instrument operating conditions and analytical procedures were: beam diameter: 3 μm;

Table 2
Whole-rock trace element contents (in ppm) of BIF macrobands #15 and #16 (<dl: below detection limit).

|	dl	BIF-15	BIF-15	BIF-15	BIF-15	BIF-15	Avg BIF-15	BIF-16	BIF-16	BIF-16	BIF-16	BIF-16	Avg BIF-16	Avg Tot
Li	0.3	0.43	0.42	0.40	–	–	0.42	0.58	0.54	–	–	–	0.56	0.47
Be	0.1	0.58	0.57	0.68	–	–	0.61	0.52	0.51	–	–	–	0.52	0.57
Na	0.5	95.79	85.89	86.94	–	–	89.54	78.83	80.51	–	–	–	79.67	85.59
Mg	2	17,010.10	17,511.66	17,650.17	6489.02	12,819.38	14,296.07	10,751.55	12,518.16	2441.41	9378.69	9889.56	8995.87	11,645.97
Al	0.2	16,752.45	13,722.18	13,734.48	–	–	14,736.37	7238.46	8706.50	–	–	–	7972.48	12,030.81
P	5	117.56	126.79	130.25	73.92	40.21	97.75	266.89	210.25	211.34	142.63	80.54	182.33	140.04
K	6	276.57	220.26	218.13	–	–	238.32	166.40	191.75	–	–	–	179.08	214.62
Ca	31	535.47	488.08	484.19	1053.59	359.84	584.23	1326.66	1079.23	1012.37	720.77	2645.32	1356.87	970.55
Ti	0.09	3.44	3.85	3.58	–	–	3.63	8.62	7.86	–	–	–	8.24	5.47
Sc	0.1	–	–	–	<dl	<dl	<dl	–	–	<dl	<dl	0.44	0.44	0.44
V	0.05	1.12	1.19	1.20	1.52	1.03	1.21	0.92	0.94	1.17	0.66	1.43	1.02	1.12
Cr	0.05	3.26	4.45	4.49	0.79	0.45	2.69	1.96	1.96	0.99	0.80	2.90	1.72	2.20
Mn	0.03	170.04	195.84	198.08	26.52	47.30	127.56	273.75	323.53	64.02	83.15	296.36	208.16	167.86
Fe	3.7	191,354.86	256,487.82	259,137.03	303,691.59	195,296.52	241,193.56	284,666.83	291,940.09	302,678.24	121,550.20	181,472.69	236,461.61	238,827.59
Co	0.06	0.33	0.26	0.26	0.49	0.31	0.33	0.29	0.35	0.85	0.66	0.86	0.60	0.47
Ni	0.06	1.27	1.71	1.72	1.36	0.96	1.40	0.74	0.84	2.23	1.64	1.78	1.45	1.43
Cu	0.03	1.18	1.04	0.44	0.51	1.90	1.01	0.48	0.50	1.86	3.02	5.30	2.23	1.62
Zn	0.08	11.95	9.25	9.15	4.64	15.47	10.09	8.91	9.31	3.05	6.87	14.41	8.51	9.30
Ga	0.01	0.13	0.13	0.14	–	–	0.14	0.14	0.13	–	–	–	0.14	0.14
As	0.06	0.39	0.44	0.44	1.50	1.34	0.82	0.99	0.89	1.10	0.56	0.36	0.78	0.80
Rb	0.04	2.16	1.80	1.79	0.80	1.02	1.51	1.68	1.79	2.10	2.92	1.95	2.09	1.80
Sr	0.03	3.60	3.57	3.57	4.67	3.82	3.85	8.39	6.33	10.27	5.95	4.27	7.04	5.44
Y	0.02	1.62	1.62	1.63	2.17	1.62	1.73	3.21	2.45	3.15	1.62	2.71	2.63	2.18
Zr	0.09	0.72	0.76	0.76	3.81	1.84	1.58	1.50	1.30	2.22	3.71	4.66	2.68	2.13
Nb	0.04	0.07	0.08	0.08	–	–	0.08	0.19	0.12	–	–	–	0.16	0.11
Mo	0.08	0.76	0.33	0.34	0.23	0.14	0.36	0.33	0.28	0.25	0.23	0.26	0.27	0.32
Ag	0.01	0.01	0.25	0.25	0.09	0.08	0.14	0.04	0.02	0.09	0.07	0.11	0.06	0.10
Cd	0.06	<dl	<dl	<dl	<dl	<dl	<dl	<dl	<dl	<dl	<dl	<dl	<dl	<dl
Sn	0.06	0.35	0.45	0.43	–	–	0.41	0.30	0.30	–	–	–	0.30	0.37
Sb	0.01	0.25	0.26	0.26	–	–	0.25	0.55	0.35	–	–	–	0.45	0.33
Te	0.02	<dl	<dl	<dl	–	–	<dl	<dl	<dl	–	–	–	<dl	<dl
Cs	0.02	0.37	0.34	0.33	0.17	0.15	0.27	0.36	0.40	0.51	0.48	0.12	0.37	0.32
Ba	0.03	14.41	16.56	16.61	22.95	9.73	16.05	26.56	28.38	34.53	30.24	22.79	28.50	22.28
La	0.03	0.64	0.75	0.75	1.26	0.63	0.81	0.85	0.72	0.92	0.71	0.64	0.77	0.79
Ce	0.03	0.98	1.15	1.15	2.03	1.09	1.28	1.08	0.94	1.31	1.21	1.06	1.12	1.20
Pr	0	0.11	0.13	0.13	0.22	0.12	0.14	0.12	0.10	0.15	0.14	0.12	0.13	0.13
Nd	0.03	0.46	0.54	0.54	0.93	0.50	0.59	0.50	0.44	0.64	0.57	0.49	0.53	0.56
Sm	0.04	0.09	0.10	0.10	0.18	0.10	0.11	0.10	0.08	0.15	0.12	0.12	0.11	0.11
Eu	0.03	0.04	0.05	0.05	0.07	0.04	0.05	0.04	0.04	0.06	0.05	0.05	0.05	0.05
Gd	0.03	0.15	0.16	0.16	0.26	0.14	0.18	0.16	0.14	0.21	0.15	0.19	0.17	0.17
Tb	0.03	<dl	<dl	<dl	0.03	<dl	0.03	<dl	<dl	0.03	<dl	0.03	0.03	0.03
Dy	0.04	0.19	0.20	0.20	0.22	0.13	0.19	0.26	0.21	0.21	0.13	0.24	0.21	0.20
Ho	0.02	0.05	0.05	0.05	0.05	0.03	0.05	0.07	0.06	0.06	0.03	0.07	0.06	0.05
Er	0.04	0.17	0.18	0.18	0.17	0.11	0.16	0.24	0.20	0.20	0.12	0.29	0.21	0.18
Tm	0.01	0.03	0.03	0.03	0.02	0.02	0.03	0.04	0.03	0.03	0.02	0.06	0.04	0.03
Yb	0.05	0.24	0.24	0.24	0.23	0.20	0.23	0.25	0.22	0.28	0.17	0.49	0.28	0.26
Lu	0.04	0.05	0.05	0.05	<dl	<dl	0.05	0.04	0.04	0.05	<dl	0.09	0.06	0.05
Hf	0.05	<dl	<dl	<dl	0.19	0.06	0.13	<dl	<dl	0.08	0.18	0.30	0.18	0.16
Ta	0.02	<dl	<dl	<dl	–	–	<dl	<dl	<dl	–	–	–	<dl	<dl
W	0.08	0.47	0.54	0.51	–	–	0.51	0.90	0.78	–	–	–	0.84	0.64
Re	0.01	<dl	<dl	<dl	<dl	<dl	<dl	<dl	<dl	<dl	<dl	<dl	<dl	<dl
Au	0.01	0.07	0.06	0.05	–	–	0.06	0.29	0.10	–	–	–	0.20	0.11
Tl	0.05	<dl	<dl	<dl	–	–	<dl	<dl	<dl	–	–	–	<dl	<dl
Pb	0.03	0.26	0.25	0.25	0.32	0.45	0.31	0.41	0.38	0.43	0.43	0.57	0.44	0.38
Th	0.01	0.03	0.02	0.02	0.06	0.03	0.03	0.11	0.06	0.06	0.05	0.15	0.08	0.06
U	0.03	<dl	<dl	<dl	<dl	<dl	<dl	<dl	<dl	<dl	<dl	0.04	0.04	0.04
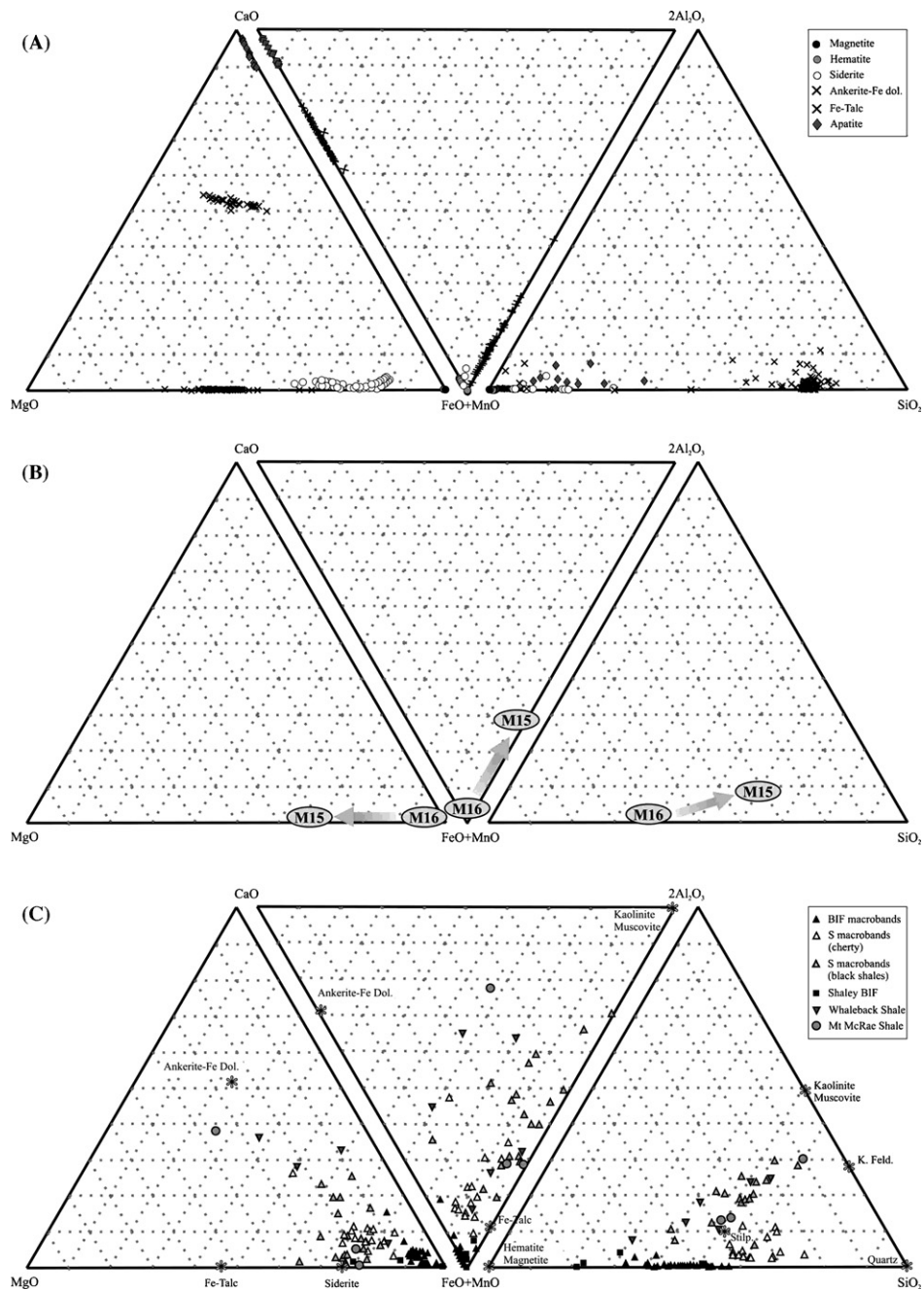
Fig. 2. Ternary diagrams displaying the chemical composition of minerals and BIF samples from the Dales Gorge Member and related rocks in terms of molecular percentages of SiO_2, Al_2O_3, $Fe_2O_3 + MnO$, CaO and MgO. (A) Compositional representation of mineral phases present in BIF macrobands #15 and #16. (B) Whole-rock analyses for BIF macrobands #15 and #16. Note that macroband #15 contains more MgO, SiO_2 and, although slightly, Al_2O_3. This enrichment is largely dictated by relative proportions of siderite and ferroan-talc, the latter being more abundant in macroband #15. (C) Dales Gorge BIF and S macrobands and associated shales (see Fig. 1). Note the different trends according to the relative abundance of diverse mineral phases present in these rocks (*sources*: Ewers and Morris, 1981; Webb et al., 2003; Alibert and McCulloch, 1993; and this study).

accelerating voltage: 15 kV; current: 15 nA; and a ZAF matrix correction was used to calculate the concentrations. In situ trace element analyses were obtained on samples 40 μm in diameter using a Quad-ICP-MS coupled to a laser ablation system. Optimization of ICP-MS instrument parameters (RF power 1200 W, peak hopping acquisition, 50 ms dwell time) was achieved by ablating the NIST SRM 610 (~500 ppm Ni) international glass standard. For quantitative trace element determinations, the NIST 610 standard and BIF samples were ablated using identical conditions with spot sizes of 40 μm, 5 Hz repetition rate and energy density of ~13 J/cm². Quantitative results were obtained via the calibration of relative element sensitivities against the NIST 610 standard, and normalization of each analysis to the electron microprobe data for Mg and Fe as the internal standards. Data reduction and concentration determinations were obtained using the GLITTER® (XP version, New Wave Research) laser ablation software. Repeated analysis (*n* = 10) of the NIST 610 using a 40 μm spot size yielded relative standard deviations of between 5 and 15% (2σ level) and detection limits between 0.2 ppm (e.g., Cu) and 3 ppm (e.g., Cr) for most elements (except for P ~13 ppm, Fe ~20 ppm, and Ca ~165 ppm). All the detailed analyses were performed at the University of Alberta, Department of Earth and Atmospheric Sciences.
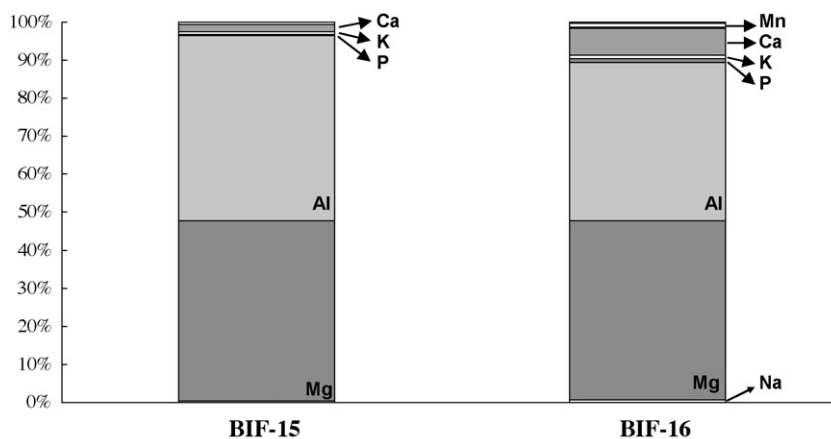
6 *E. Pecoits et al. / Precambrian Research xxx (2009) xxx–xxx*
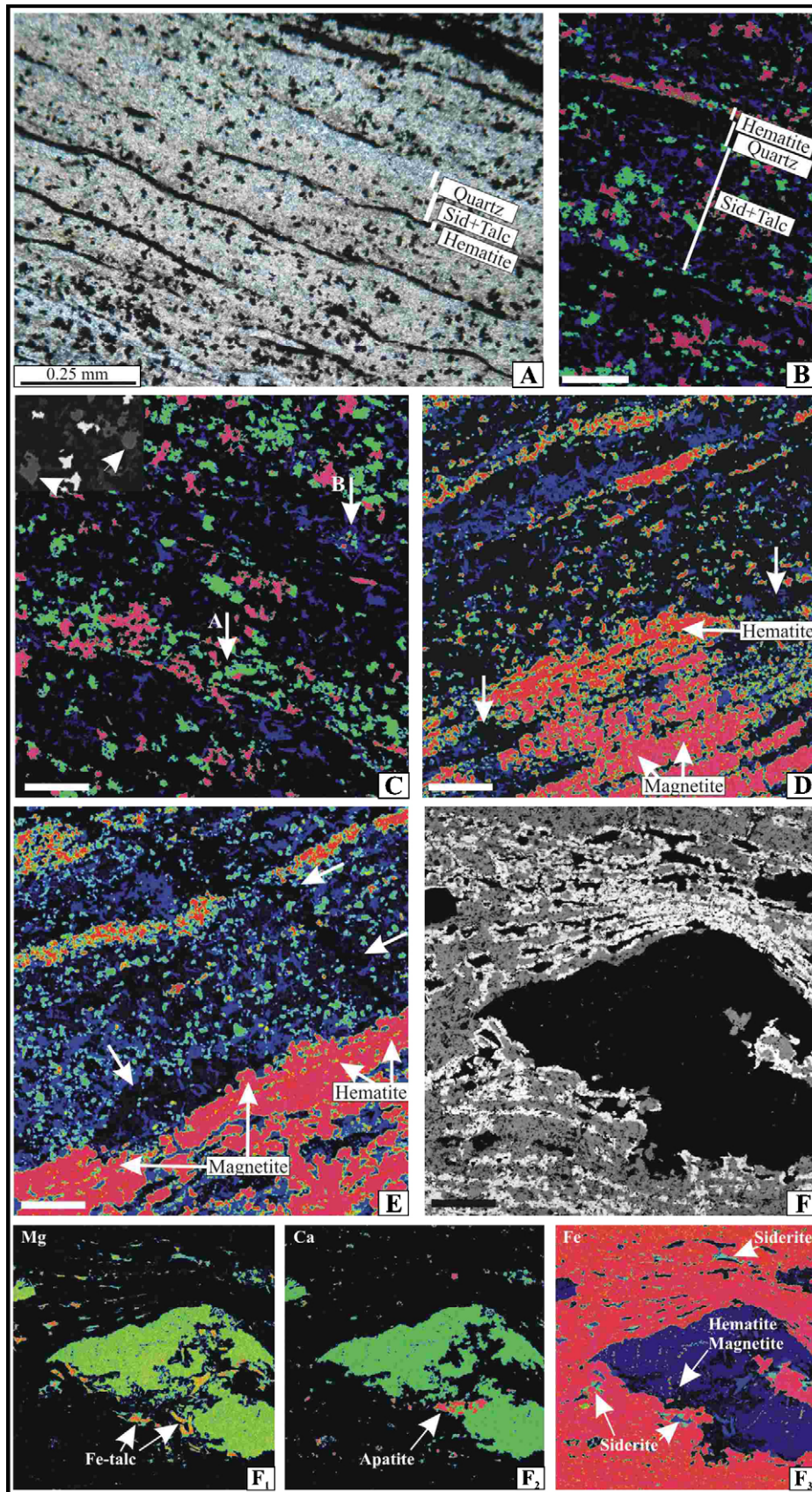
Fig. 4. Major element composition of BIF macrobands #15 and #16. Silicon and Fe are not plotted.

3. Results

3.1. Petrography

The mineralogy of the Dales Gorge BIF consists of hematite, magnetite, siderite, ferroan-talc, ankerite-ferroan dolomite, apatite and chert (Table 1 and Fig. 2). Both macrobands have the same mineralogy, however, the modal proportion of minerals and, particularly, the texture are different as a consequence of minor differences in the paragenetic sequence. The fine and regular millimeter-scale lamination (microbanding) in our samples is largely defined by the relative abundance of Fe-oxides. Contacts between "iron-rich" and "iron-poor" microbands are usually sharp (Fig. 3A), but more diffuse transitions within the "iron-poor" laminae are observed (e.g., Fig. 3B and C).

3.1.1. Hematite

In both BIF macrobands studied here, 'iron-rich' laminae are largely composed of hematite, however, different textures can be recognized. In macroband #16, massive anhedral aggregates and relatively coarse xenomorphic hematite ($\sim$100 μm) are the most common variety (Fig. 3B and C). Small xenomorphic crystals (<20 μm) are typical in macroband #15, but sporadic minute platy grains (5–15 μm) also occur (Fig. 3D and E). Hematite-rich microlaminae composed of massive aggregates tend to form more compacted and continuous layers. Locally, these massive microlayers are discontinuous and small xenomorphic crystals are more abundant in diffuse areas (Fig. 3D). Hematite crystals are found in close association with siderite grains, either with crystal face contacts or as inclusions (Fig. 3B–E).

3.1.2. Magnetite

In both macrobands, magnetite tends to occur as limpid subhedral to euhedral medium-grained crystals. However, magnetite is more abundant in macroband #16 than macroband #15. In the latter, magnetite typically occurs as subhedral overgrowths on hematite, although euhedral habit is also observed. Magnetite overgrowths are characteristically present in thicker laminae, particularly around relicts of siderite-chert microlayers (Fig. 3F). In macroband #15, such overgrowths are also present, although it is more common to observe magnetite forming nearly continuous microlayers (Fig. 3D and E). The greater abundance of magnetite in macroband #15 is accompanied by an increase in ferroan-talc and by diminished siderite content (compare Fig. 3C and D).

3.1.3. Siderite

In macroband #16, siderite crystals are fine to medium-grained in size (average $\sim$0.035 mm). They are present as subhedral rhomboids, sometimes showing the development of rims, although the edges commonly display corrosion gulfs resulting in a xenomorphic morphology (Fig. 3B and C). The grains contain a clear core and terminate with bright micron-scale rims of uniform thickness that are relatively enriched in Fe (Fig. 3C, inset). The boundary between the core and the rim is characterized by irregular to straight edges indicating a dissolution event prior to, or concurrent with, rim precipitation. Macroband #15 consists of very fine-grained anhedral siderite (0.02 mm in diameter) without rims (Fig. 3D and E). Hematite and chert inclusions are commonly present.

3.1.4. Ferroan-talc

Talc is ubiquitous in all thin sections analyzed, but is most abundant in samples from macroband #15. Fig. 3C and D illustrate the characteristic habit of ferroan-talc, which occurs as subhedral sheaves. The sheaves are found randomly oriented among the finely crystalline chert matrix and locally perpendicular to the microbanding. Although similar features have been seen in both macrobands, samples from macroband #15 display more abun-

Fig. 3. Microphotographs, microprobe elemental maps and backscattered images illustrating varied textures of the BIF macrobands #15 and #16 from Dales Gorge Member (all scale bars: 200 μm) (see text for explanation). (A) Microphotography of finely laminated BIF where iron-'rich' microbands are defined by hematite ($\pm$magnetite) and iron-'poor' microbands by siderite-Fe-talc-chert (and hematite) interbedded with occasional pure chert microlayers. (B) Electron microprobe map of Fe showing a close-up view of similar banding style with cycles as thin as 300–400 μm (BIF macroband #16). Note the rhythmic distribution of hematite (red), chert (black), siderite (green) and Fe-talc (blue). (C) Typical texture of macroband #16 illustrating xenomorphic hematite and siderite, Fe-talc and chert (colors of the minerals as in B). Note the abundant inclusions of hematite + chert in siderite grains (arrow A) and hematite + siderite in Fe-talc (arrow B). Inset: backscattered image showing thin rims around siderite grains (FOV = 200 μm). (D) Partially dissolved hematite–magnetite microbands. Note that fine-grained siderite crystals without rims and the fairly continuous banding defined by randomly oriented sheaves of Fe-Talc (compare with B and C) (BIF macroband #15). (E) Characteristic texture of BIF macroband #15 showing abundant Fe-talc, overgrowths of magnetite (pink) on laminated xenomorphic hematite (red). Note the smaller size of siderite and hematite when compared with BIF macroband #16 (Fig. 3C). Arrows indicate interruptions in the microbanding. (F) Backscattered image with accentuated contrast illustrating overgrowth of magnetite (white) on hematite (grey) and a large ankerite-Fe dolomite – clearly deforming the iron oxide microlaminae – associated with Fe-rich microbands. Elemental maps of Mg, Ca and Fe (insets F_1, F_2 and F_3) depict inclusions of hematite, magnetite, Fe-talc and apatite. Inset F_3 shows the presence of siderite in the chert-rich microband relicts around which magnetite is developed (macroband BIF #16). (For interpretation of the references to color in this figure legend, the reader is referred to the web version of the article.)
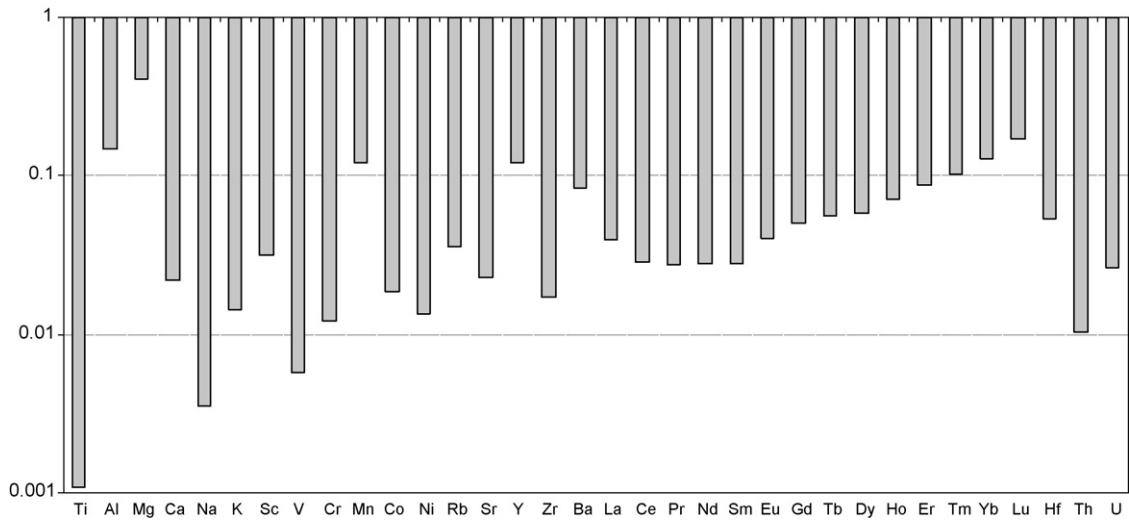
Fig. 5. Depletion–enrichment diagram of BIF macrobands #15 and #16 as compared to upper Archaean crust data of Taylor and McLennan (1985).
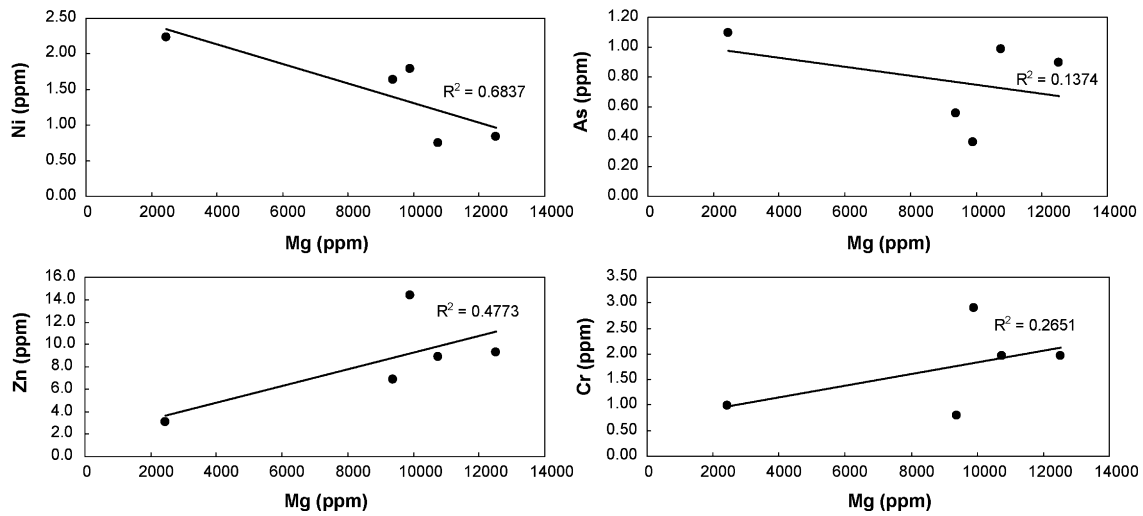

Fig. 6. Plots of Mg vs. various trace elements for the macroband #15.
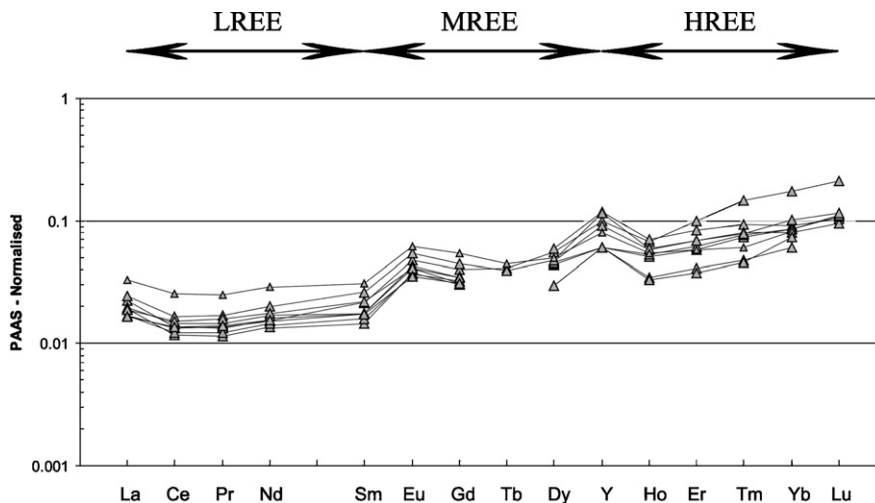

Fig. 7. PAAS-normalized REY pattern for Dales Gorge BIF macrobands #15 and #16. The same trends are obtained using MUQ (Mud from Queensland) of Kamber et al. (2005). Thus, irrespective of the normalization method (PAAS or MUQ), the normalized pattern displays remarkably similar trends.

Table 3
Electron microprobe analysis (in wt%) of BIF macrobands #15 and #16 from Dales Gorge Member.

	Hematite (n = 58)			Magnetite (n = 56)			Siderite (n = 85)			Ferroan-talc (n = 68)			Apatite (n = 10)			Ankerite-Fe Dol. (n = 31)		
	Avg	Min	Max	Avg	Min	Max	Avg	Min	Max	Avg	Min	Max	Avg	Min	Max	Avg	Min	Max
K_2O	0.021	0.000	0.054	0.008	0.000	0.026	0.006	0.000	0.023	0.073	0.000	0.759	0.002	0.000	0.010	0.005	0.000	0.018
Na_2O	0.033	0.005	0.087	0.030	0.000	0.080	0.020	0.000	0.066	0.036	0.000	0.257	0.427	0.244	0.797	0.013	0.000	0.049
CaO	0.023	0.000	0.057	0.020	0.006	0.051	0.790	0.114	1.761	0.053	0.004	0.138	53.52	50.79	55.38	27.47	13.40	29.36
SiO_2	0.764	0.218	1.286	0.510	0.183	2.065	2.499	0.081	9.113	54.52	32.88	61.70	0.907	0.269	2.914	3.333	0.087	31.577
FeO	86.37	85.42	87.68	90.41	86.48	91.43	41.96	26.37	46.36	16.66	11.83	23.55	3.45	1.41	5.61	13.20	10.06	16.66
P_2O_5	0.015	0.000	0.053	0.014	0.000	0.076	0.013	0.000	0.058	0.011	0.000	0.057	38.43	36.93	39.60	0.011	0.000	0.038
MgO	0.106	0.023	0.298	0.045	0.009	0.478	12.29	6.16	18.26	18.79	11.98	22.79	0.230	0.022	0.484	13.52	10.70	17.04
Cl	0.009	0.000	0.033	0.012	0.000	0.037	0.006	0.000	0.025	0.007	0.000	0.026	0.085	0.037	0.164	0.007	0.000	0.029
Al_2O_3	0.055	0.003	0.944	0.018	0.000	0.053	0.031	0.000	0.490	0.750	0.038	3.850	0.078	0.005	0.190	0.032	0.000	0.265
MnO	0.011	0.000	0.039	0.014	0.000	0.053	0.418	0.177	0.786	0.014	0.000	0.042	0.038	0.006	0.066	0.351	0.175	0.496

dant crystalline aggregates, typically observed as radiating splays (Fig. 3D and E). Siderite and hematite inclusions have also been observed (Fig. 3C). Locally, regular microlaminae of finely matted intergrowth of thin sheaves have been recorded directly overlying the Fe-oxides bands (Fig. 3D).

3.1.5. Ankerite-ferroan dolomite

Ankerite-ferroan dolomite is not as abundant as the aforementioned minerals; it was only observed in macroband #16 and is restricted to thick Fe-rich microbands. Its poikilotopic texture, including hematite, magnetite, ferroan-talc and apatite relicts, indicates that it formed after the minerals it includes (Fig. 3F). It also distorts the sedimentary microlamination around it, suggesting prelithification deformation. Mg/Fe ratios of these carbonates are consistent with an ankerite composition (Fig. 2A).

3.1.6. Apatite

Scarce, massive and characteristically anhedral apatite grains have been identified preferentially related to iron oxides microbands, although relatively large (120 μm) subhedral crystals and occasional extremely fine-grained (10 μm) varieties also occur. Small inclusions of hematite are present within the massive apatite. Similar to siderite, the crystals exhibit variably corroded faces. Euhedral diagenetic overgrowths are absent.

3.1.7. Chert

Chert occurs interbedded with Fe-rich microbands, constituting the most abundant mineral phase. It is found in conjunction with siderite, ferroan-talc and minor hematite, but pure silica underlying Fe-oxide microlaminae is also observed (Fig. 3B). Hematite, magnetite and siderite normally display inclusions of chert trapped during crystal growth or due to coalescence of Fe-oxide rich microlaminae.

3.2. Geochemistry

For the purpose of this study, 10 whole-rock trace element analyses (five in each macroband) were performed. Furthermore, approximately 300 electron microprobe analyses and more than 150 LA-ICP-MS analyses were carried out with the aim of establishing the trace element distribution within different minerals of the Dales Gorge BIF. In this regard, both the whole-rock and the microscale chemical analyses were performed in the same stratigraphic position.

3.2.1. Bulk chemical analyses

Whole-rock chemical data is presented in Table 2. Major components are Si and Fe, followed by lesser amounts of Mg, Al, Ca, K, Na, Mn and P (Fig. 4). Samples with higher Fe contents tend to have lower Mg, Al, Ca, K, and Na values (Fig. 2). These trends indicate more abundant ferroan-talc and carbonates (siderite and ankerite-ferroan dolomite) at the expense of iron oxides (hematite and magnetite). The presence of Al indicates that Fe-silicates were present in the precursor minerals assemblages because only silicates (e.g., greenalite) can accept relatively elevated amounts of Al into their structures. Potassium and Na show highly positive correlations with Al ($r^2 = 0.91$). Correlations between these elements are to be excepted as they also occur only in silicates. However, the negative correlations between Ti and Cr ($r^2 = 0.8$), and Al with Ti ($r^2 = 0.9$), as well as the extremely low concentrations of Th (<0.16 ppm), Hf (below detection limit) and Sc (below detection limit), reflect a non-detrital origin for the inferred silicates.

Trace elements typically occur in low concentrations (<35 ppm) compared to the average Archean crust. These include transition trace metals (Sc, V, Cr, Co, Ni), high field strength elements (Y,

Table 4

Trace element concentrations (in ppm) of BIF macrobands #15 and #16 from Dales Gorge Member (NM: not measured).

	Hematite (n = 70)			Magnetite (n = 28)			Siderite (n = 32)			Ferroan-talc (n = 11)			Apatite (n = 5)			Ankerite-Fe Dol. (n = 6)		
	Avg	Min	Max	Avg	Min	Max	Avg	Min	Max	Avg	Min	Max	Avg	Min	Max	Avg	Min	Max
Mg	4,551	110	120,647	1,917	107	13,504	–	–	–	–	–	–	–	–	–	–	–	–
Si	23,883	798	783,458	53,157	743	613,207	432,963	26,051	809,219	596,049	59,278	884,011	31,745	741	109,188	9,619	283	39,477
P	473	97	9,476	338	64	2,871	444	43	8,467	2,729	91	10,429	10,450	290	22,807	48	19	76
Ca	19,137	795	595,004	3,743	572	17,957	6,393	3,791	46,359	56,315	2,713	144,993	31,779	3,613	64,952	208,568	200,372	221,669
Sc	5.68	2.79	16.63	4.50	1.87	8.64	–	–	–	–	–	–	–	–	–	–	–	–
V	3.96	1.75	11.60	3.25	1.62	6.53	0.60	0.29	1.53	0.73	0.25	1.07	0.05	0.01	0.11	0.35	0.31	0.41
Cr	25.03	11.91	74.38	20.37	8.93	40.03	16.18	5.75	27.03	12.65	6.96	22.19	0.73	0.11	1.80	3.96	2.16	5.64
Mn	253	6	6,332	155	8	1,589	3,113	859	4,382	1,171	32	2,984	47	26	84	2,504	2,362	2,560
Fe	680,322	675,483	684,034	715,583	714,349	716,292	258,363	138,690	642,785	165,126	112,340	280,933	6,455	2,680	9,041	97,672	66,976	129,793
Ni	11.95	1.59	47.58	10.02	1.92	21.70	–	–	–	–	–	–	–	–	–	–	–	–
Co	2.44	1.05	5.58	1.91	0.69	4.48	1.13	0.55	2.12	1.05	0.47	2.25	0.21	0.01	0.59	0.29	0.24	0.34
Cu	6.92	2.26	22.65	6.15	2.49	12.15	2.64	0.35	18.04	1.15	0.73	1.79	0.15	0.01	0.33	0.52	0.38	0.63
Zn	16.39	7.90	61.50	15.04	5.05	35.24	25.46	5.94	59.24	43.98	10.46	76.99	1.07	0.15	2.17	5.52	4.27	6.30
Ge	7.98	3.91	21.49	10.47	4.91	16.29	1.32	0.70	3.16	2.07	0.81	2.57	0.10	0.02	0.27	0.68	0.62	0.79
As	12.25	6.23	34.07	10.06	4.50	25.97	62.57	13.14	231.76	47.54	13.92	115.61	1.62	0.31	3.82	19.72	18.22	22.35
Rb	2.88	0.71	7.18	1.88	0.60	5.50	–	–	–	–	–	–	–	–	–	–	–	–
Sr	22.43	0.98	562.59	10.47	0.93	73.91	–	–	–	–	–	–	–	–	–	–	–	–
Y	10.49	0.45	218.71	6.79	0.44	61.43	–	–	–	–	–	–	–	–	–	–	–	–
Zr	2.87	0.54	15.77	2.30	0.81	7.28	–	–	–	–	–	–	–	–	–	–	–	–
Mo	2.82	0.00	10.45	2.57	0.32	6.28	0.86	0.42	1.85	0.83	0.49	1.15	0.06	0.01	0.18	0.35	0.27	0.44
Ag	2.62	1.06	7.24	2.32	0.73	5.39	–	–	–	–	–	–	–	–	–	–	–	–
Cd	5.17	1.41	16.27	4.31	1.52	11.74	–	–	–	–	–	–	–	–	–	–	–	–
Cs	1.18	0.59	3.01	0.89	0.36	1.96	–	–	–	–	–	–	–	–	–	–	–	–
Ba	65.75	7.16	155.99	24.19	4.81	109.92	–	–	–	–	–	–	–	–	–	–	–	–
Hf	1.41	0.44	3.37	1.22	0.48	2.30	–	–	–	–	–	–	–	–	–	–	–	–
Re	1.51	0.32	4.31	1.34	0.25	3.35	–	–	–	–	–	–	–	–	–	–	–	–
Pb	2.12	0.84	14.89	1.57	0.72	2.82	–	–	–	–	–	–	–	–	–	–	–	–
Th	0.53	0.13	3.16	0.40	0.13	1.45	–	–	–	–	–	–	–	–	–	–	–	–
U	0.43	0.12	1.65	0.46	0.17	0.89	–	–	–	–	–	–	–	–	–	–	–	–

Zr, Nb, Th, U, Hf, Pb), large ion lithofile elements (Ba, Sr, Rb) and REEs (cf. Taylor and McLennan, 1985) (Fig. 5). Of the main mineral phases (i.e., quartz, hematite, magnetite, ferran-talc and siderite), iron oxides and ferran-talc host the largest amount of trace metals present in the analyzed samples (see below). Accordingly, the distribution of the trace metals is mainly controlled by the relative proportion of these minerals. Samples with high Mg content are largely dominated by ferran-talc (macroband #15) whereas those with low concentration are dominated by Fe-oxides (macroband #16). In macroband #15 the negative Mg–Ca relationship ($r^2 = 0.65$) shows that Mg is highly associated with ferran-talc. Although, the macroband #16 shows a few samples with some moderately high Mg concentration, since Mg is hosted also by siderite and ankerite-ferran dolomite, it never reaches the values of macroband #15.

Fig. 6 shows the distribution of selected trace elements relative to Mg. Here, Ni and As decrease with increasing Mg. This strong negative correlation of Ni and As with Mg is a consequence of both trace elements being largely present in Fe-oxides (see mineral chemical analyses below), so that any variation in one of these components (i.e., Ni-As and Mg) will be reflected antithetically by the other. Although Ni is present in all major mineral phases, it is more abundant in the macroband #16 due to the affinity of this element with Fe-oxides relative to other mineral species. Conversely, Zn and Cr show highly positive correlations because these two elements are dominantly present in ferran-talc. The rest of the trace elements appear to have no pattern in their distribution. Regarding bioessential metals, such as Mo, Cu, V and Cd, their concentrations are below 3 ppm, whereas P reaches values up to 270 ppm.

Figs. 7 and 8 show the rare earth element plus yttrium (REY) concentrations. Their patterns are characterized by: (i) depleted LREE relative to MREE and HREE ($Pr/Yb_{SN} = 0.08–0.3$), and depleted MREE relative to the HREE ($Sm/Yb_{SN} = 0.1–0.4$); (ii) distinct positive La anomalies ($La/La^* = 2.1 \pm 0.5$); (iii) Eu enrichment relative to neighbouring REE ($Eu/Eu^* = 1.6 \pm 0.1$); and (iv) Y enrichment relative to Ho, yielding strongly superchondritic Y/Ho ratios (42 ± 12). Except for the differences in the Eu and Ce anomalies, the latter being absent in all the samples analyzed here, they have similar trends to present day seawater in terms of their overall REE patterns (e.g., Bolhar et al., 2004); i.e., positive Y and Gd anomalies and LREE < MREE < HREE ($Gd_{SN}/Tb_{SN} < 1$; $La_{SN}/Yb_{SN} < 1$). For the studied samples, crustal contamination is discounted on the basis of the low concentrations of Th (0.02–0.15 ppm), Zr (0.7–4.7 ppm), Hf (0–0.3 ppm) and Sc (0–0.44 ppm), as well as the lack of co-variations of Zr vs. Y/Ho, Y/Ho vs. Ce/Ce* and Th vs. La/La*. Furthermore, when plotted in Ce/Ce* vs. Pr/Pr* diagram, all the samples overlap with other correlative Palaeoproterozoic BIFs (Fig. 8A).

3.2.2. Mineral chemical analyses

Major and trace element concentrations of the minerals described above are summarized in Tables 3 and 4 and Fig. 9. Even though all mineral phases reported here have been identified in both sets of samples, only those minerals present in elemental distribution map areas were chemically analyzed. Therefore, for macroband #15, no geochemical data is available for apatite and only one ankerite crystal was analyzed. No discernable vertical trends in trace element concentrations have been recorded for any mineral phases.

3.2.2.1. Hematite. As predicted, the highest concentration of Fe (wt% as total FeO) is observed in hematite (85.4–87.7) and magnetite (see below). Manganese, most likely substituting for Fe, is very low (<0.51 wt%), with most values being <0.30 wt%. Even though few analyses show MgO concentrations above 0.19 wt%, it corresponds to increasing SiO$_2$ content (<1.3 wt%) and probably represents contamination by ferran-talc. Insignificant concentrations
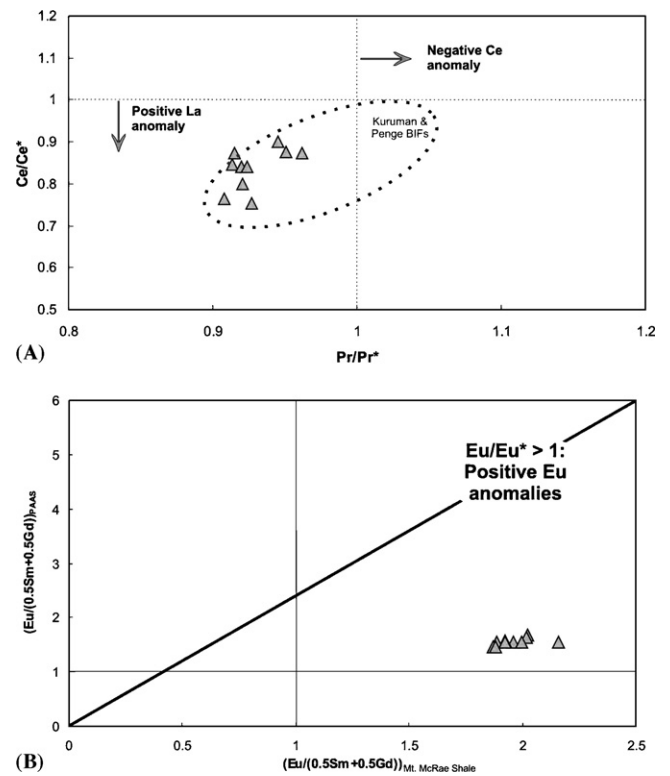

Fig. 8. (A) Plot of Ce/Ce* vs. Pr/Pr* showing a positive La but no Ce anomaly. Dales Gorge samples fit in the field depicted by BIFs from the Kuruman and Penge Iron Formations (see Bau and Dulski, 1996). (B) The positive Eu anomaly recorded in the Dales Gorge BIF (see Fig. 7) is still present when PAAS are normalised using directly overlying Mt. McRae shale; arguing against any artificial anomaly (see Bolhar et al., 2004).

of Al (0.09 wt%) were detected, possibly reflecting ionic substitution for Fe in the structure. Ba, Cr and Sr are the most abundant trace elements present in hematite with averages of 66, 25 and 22 ppm, respectively. These are followed by Zn, Ni, As, Y and Cu, with average concentrations between 7 and 16 ppm. Hematite contains the highest measured values of Sr (563 ppm), Y (219 ppm), Ba (156 ppm), Cr (75 ppm), Ni (48 ppm), Cu (23 ppm), Ge (21 ppm), Zr (16 ppm), and Mo (11 ppm). All other trace elements, (Sc, V, Co, Ge, Rb, Zr, Mo, Ag, Cd, Cs, Hf, Re, Pb, Th and U), tend to be present in concentrations <10 ppm. High P values (correlated with elevated Ca) are likely due to contamination by minute apatite grains.

3.2.2.2. Magnetite. Magnetite contains the highest Fe (wt% as total FeO) content, between 90.03 and 91.98%. In contrast to hematite it has low MgO values (<0.09 wt%) that do not correlate with SiO$_2$ content. Similar to hematite, it is characterized by similar trends of Al$_2$O$_3$, K$_2$O, NaO, CaO, P$_2$O$_5$, and Cl, most of them comprising less than 0.005 wt%. It also contains relatively significant, but lower, average concentrations of Ba (24 ppm), Cr (20 ppm) and Sr (10 ppm). Likewise, Zn (15 ppm), Ni (10 ppm), As (10 ppm), Y (7 ppm) and Cu (6 ppm) are the next most important trace elements. Except for Ge (10 ppm), the other trace elements have concentrations generally <4 ppm, although sporadically some of them show maximum values as high as 12 ppm (e.g., Cr).

3.2.2.3. Siderite. Siderite composition is approximately ($Fe_{0.6–0.75}Mg_{0.25–0.4}$)CO$_3$. FeO concentrations in siderite range from 26.4 to 46.4 wt% (Table 3). Magnesium oxide is the next most abundant component, ranging from 6.2 to 18.3 wt%, with lower values corresponding to higher FeO contents. This negative correlation evidences Mg substitution for Fe. Likewise, both Mn
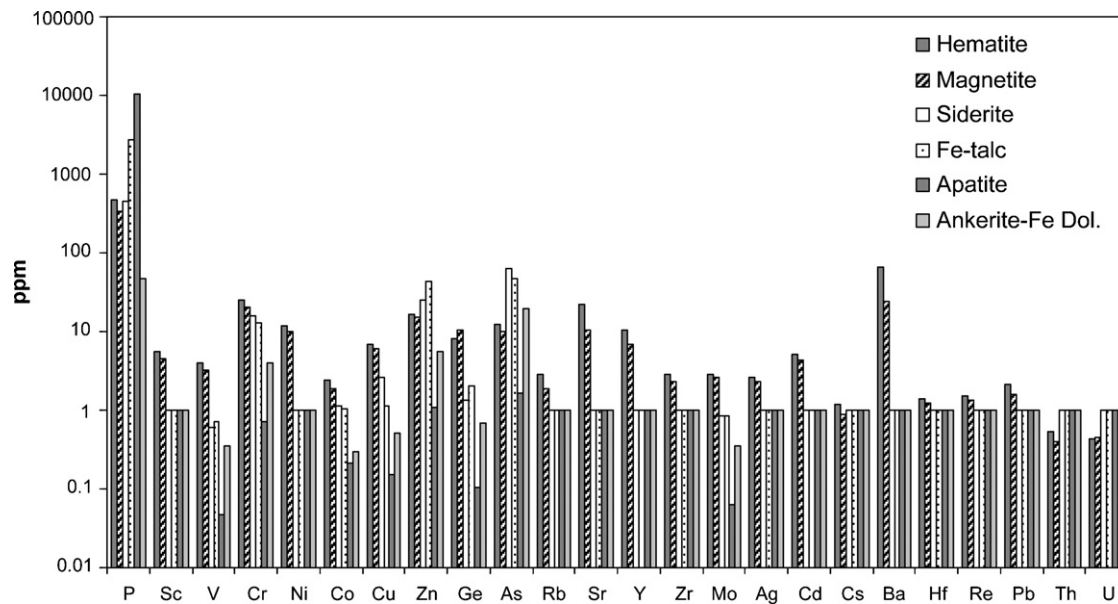
E. Pecoits et al. / Precambrian Research xxx (2009) xxx–xxx

Fig. 9. Trace element concentrations in specific mineral phases present of macrobands #15 and #16.

(0.13–0.90 wt%), which reaches the highest abundance in this phase, and Ca (0.18–2.03 wt%), substitute for Fe. Likely due to the large difference in size between Ca and Fe, this substitution appears to be limited. Of the trace metals analyzed, siderite contains significant amounts of As, Zn and Cr, with average values of 62, 25 and 16 ppm, respectively. It also contains the highest As (232 ppm) concentrations recorded.

3.2.2.4. Ferroan-talc. The almost complete substitution of iron by magnesium (minnesotaite) is a common feature in the talc component of several iron formations (e.g., Klein, 2005); partial substitutions are also common. In this study, FeO and MgO contents were determined for 68 crystals with ranges from 11.8 to 23.6 (wt%) and from 12 to 22.8 (wt%), respectively. Manganese (MnO) concentrations are low, indicating very little substitution for Mg. Calcium (CaO) and the alkalis ($Na_2O–K_2O$) are probably present as interlayer ions or as impurities, however, they may also substitute for magnesium. Electron microprobe analyses show variable quantities of Al ranging from 0.04 to 3.9 (Al_2O_3, wt%), which commonly substitutes for Si (Deer et al., 1962). Similar to siderite, As is the most abundant trace element and reaches average values of 48 ppm and concentrations as high as 116 ppm. Zn is the next most abundant trace metal, reaching up to 77 ppm, and it appears to be largely associated with ferroan-talc. Cr also shows a relatively high abundance, with average values of 13 ppm and maximum concentrations up to 22 ppm.

3.2.2.5. Ankerite-ferroan dolomite. This mineral phase ranges in composition from ferroan dolomite ($CaMg_{0.8}Fe_{0.2}(CO_3)_2$) to magnesian ankerite ($CaMg_{0.5}Fe_{0.5}(CO_3)_2$). Variations in Fe content (10.0–16.7 wt% FeO) are directly related to the Mg content (10.7–17.0 wt% MgO), with the lowest values of Fe corresponding to the highest concentrations of Mg. Mn (0.2–0.5 wt% MnO) correlates positively with Fe and negatively with Mg, suggesting that Mn preferentially replaces Mg in the structure. The Ca contents are variable, ranging from 13.4 to 29.4 wt% (CaO). Despite the narrow range, higher values of Ca are generally associated with crystals possessing relatively high concentrations of Mg. Considering both the low number of LA-ICP-MS analyses performed for this phase and that only two crystals were analyzed, the evidence presented here is not conclusive, nevertheless, some noteworthy observations can

be made. Notably, as for the aforementioned minerals, ankerite-ferroan dolomite consistently contains high concentrations of As (18–22 ppm) relative to the other trace elements. Cr and Zn are present in approximately equal concentration (∼5 ppm). Anomalously high quantities of P (up to 76 ppm), are a result of apatite crystals present as inclusions within ankerite-ferroan dolomite.

3.2.2.6. Apatite. The P_2O_5 is primarily associated with apatite (36.93–39.60 wt%). Likewise, apatite has the highest Ca contents (50.8–55.4 wt% CaO) and the lowest Fe contents (1.4–5.6 wt% FeO) of all the analyzed minerals. Although low concentrations of most elements are observed, Na contents range from 0.2 to 0.8 wt% (Na_2O), which corresponds to the highest content recorded in this study. Apatite is also highly depleted in all trace metals measured; except for As, Zn and Cr, the trace element concentrations are <1 ppm.

4. Discussion

4.1. Paragenetic sequence

This petrographic and geochemical study of the Dales Gorge Member BIF allows us to establish different stages of mineral generation and assess the diagenetic modifications of the likely initial precipitates (Fig. 10). Chert layers occur as nearly pure quartz, but can contain ferroan-talc, siderite and minor hematite. This suggests that the primary silicate precipitate was amorphous silica with cyclic contributions from dissolved Mg–Fe–Ca and HCO_3. Some amorphous silica would have crystallized as pure chert, while the latter combinations would have led to greenalite (precursor of ferroan-talc) and siderite, respectively. The relative proportions and sometimes cyclic alternation of these minerals (i.e., chert, siderite and ferroan-talc) within the 'silica-rich' bands most likely reflects variable pCO_2 (Konhauser et al., 2007b) or the result of turbiditic flows (Krapež et al., 2003; Pickard et al., 2004). Alternatively, the tripartite subdivision of the microbands (see Fig. 3A and B): Fe-oxide, chert-siderite-talc, and pure chert could represent a diagenetic feature whereby the precipitation/sedimentation of a rather homogenous mass of silica gel was followed by ion diffusion with the consequent segregation of laminae. The precise nature of this very fine-scale lamination is out of the scope of this study but certainly, more research is needed.
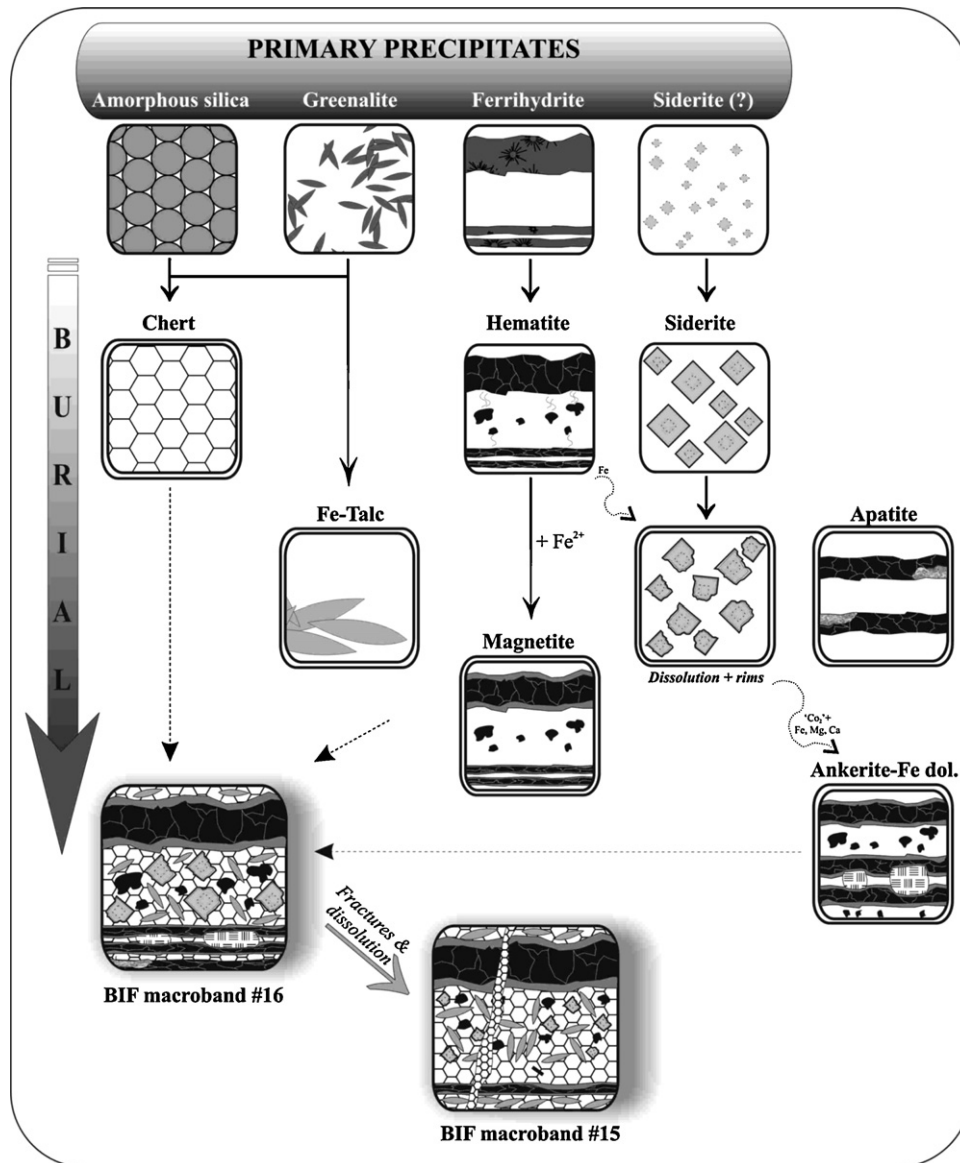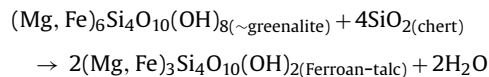
Fig. 10. Schematic paragenetic sequence for Dales Gorge BIF macrobands #15 and #16 (see text for explanation).

Based on petrographic evidence, greenalite became unstable and was entirely transformed into ferroan-talc, likely by the mechanism:

$$(Mg, Fe)_6 Si_4 O_{10}(OH)_{8(\sim greenalite)} + 4SiO_{2(chert)}$$

$$\rightarrow 2(Mg, Fe)_3 Si_4 O_{10}(OH)_{2(Ferroan-talc)} + 2H_2 O$$

In addition, as clearly observed in macroband #15, ferroan-talc is also a reaction product of siderite and chert:

$$3(Fe, Mg)CO_{3(siderite)} + 4SiO_{2(chert)} + H_2 O$$

$$\rightarrow (Mg, Fe)_3 Si_4 O_{10}(OH)_{2(Ferroan-talc)} + 3CO_2$$
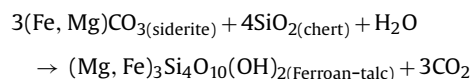
Although well preserved, our samples do not contain relevant metamorphic mineral assemblages to unambiguously ascertain the maximum temperature and pressure. According to Ewers and Morris (1981) variations in mineralogical assemblages suggest increasing metamorphic grade from Paraburdoo to Wittenoom (i.e., from the center of the BIF depositional basin to the margins). Based on oxygen-isotopic analyses, Becker and Clayton (1976) concluded maximum burial temperatures between 270 and 310 °C for

Wittenoom area (see also Ayres, 1972), whereas Kaufman et al. (1990) determined final equilibrium temperatures ranging from 60 to 160 °C in Parburdoo. The presence of ferroan-talc has typically been associated with late diagenesis to low-medium (biotite zone) metamorphic grade (Klein, 1983, 2005). In the studied samples, a significant proportion of ferroan-talc most likely precipitated before and during burial diagenesis as it occurs as inclusions in ankerite grains (see Fig. 3F).

Fe-oxide minerals occur most commonly in well-defined continuous microlaminae. Where vertical migration of fluids occurred, the dissolution of iron oxides interrupted the microlayers (Fig. 3D and E). Under those circumstances, small xenomorphic crystals most likely originated due to partial dissolution of larger crystals and aggregates. Indeed, hematite displays textural diversity, with massive anhedral aggregates, xenomorphic and rare platy grains. Although all forms may be present together, massive anhedral aggregates are characteristic of macroband #16 and small xenomorphic hematite is proportionally more abundant in macroband #15. Given its thermodynamic stability and kinetic sluggishness, the initial precipitate to hematite is likely to have been ferrihydrite,

Fe(OH)$_3$ (Glasby and Schulz, 1999; Ahn and Buseck, 1990; Dekov et al., 2007). As previously observed by Schwertmann and Murad (1983), aging of ferrihydrite at pH 4 produces goethite and minor hematite, whereas crystallization at pH 7–8 is the major pathway for hematite formation. Therefore, we suggest that hematite is a secondary mineral formed in circumneutral pH conditions after initial precipitation. Whether the initial oxidation of dissolved Fe(II) was a consequence of reaction with cyanobacterially generated O$_2$ (Cloud, 1965, 1968; James, 1988; Klein and Beukes, 1989; Morris, 1993), an inorganic photochemical reaction activated by ultraviolet light (Cairns-Smith, 1978; Braterman and Cairns-Smith, 1987) or by anaerobic photosynthetic Fe(II)-oxidizing bacteria (Widdel et al., 1993; Konhauser et al., 2002; Kappler et al., 2005) remains unresolved, and beyond the scope of this work. Recent experimental work, however, appears to rule out UV photo-oxidation as a feasible mechanism for BIFs deposition in natural seawater (Konhauser et al., 2007b).

The presence of siderite as a primary precipitate has been previously reported from the Dales Gorge Member (Kaufman et al., 1990) and Kuruman Iron Formation of the Transvaal Supergroup, South Africa (Klein and Beukes, 1989). Although some siderite may have formed penecontemporaneously, the petrographic evidence of the samples studied here suggests that the siderite growth occurred during diagenesis. For example, no optical or chemical zonation reflecting sudden changes in the precipitation environment (e.g., seawater vs. pore fluids) have been recorded. Furthermore, siderite is not found within hematite grains, whereas the presence of chert and hematite as inclusions within the siderite supports its (siderite) formation at a later stage. Noteworthy, is that there is no evidence of chert substitution by siderite as a result of hydrothermal alteration, as reported in other BIF successions (Chown et al., 2000; Mueller et al., 2009). One possibility is that siderite is the reaction product of bacterially mediated Fe(III) reduction coupled to the oxidation of organic carbon (Walker, 1984). Becker and Clayton (1972) and Baur et al. (1985) interpreted the low δ^{13}C values present in BIFs to reflect biological sources of carbon during siderite formation. Klein and Beukes (1989) observed that the Fe-oxide rich BIF in the Kuruman sequence contains less carbon than the siderite-rich BIF, thereby suggesting that the latter could not have been derived from the former by making use of organic carbon as reductant. Nonetheless, recent experimental studies on C isotope fractionation produced by Fe(III)-reducing bacteria (Romanek et al., 2003) indicate that dissolved bicarbonate produced by oxidation of organic carbon via this process generates δ^{13}C values in a similar range to those recorded in BIFs (Beukes et al., 1990; Beukes and Klein, 1990; Kaufman, 1996). Hence, the formation of siderite from precursor ferrihydrite by Fe(III)-reducing bacteria might explain the textural relationships observed here; i.e., diagenetic siderite with common hematite inclusions. As mentioned below, the latter is also supported by the light δ^{13}C values and the relatively low δ^{56}Fe values (e.g., Johnson et al., 2008).

Magnetite always occurs as overgrowths on hematite, especially along the boundaries between hematite- and chert + siderite-rich laminae (Fig. 3F). Additionally, no petrographic evidence of primary precipitation of magnetite has been documented. Hence, we believe that it formed through the conversion of hematite. Such conversion requires Fe(II), which could be sourced by; (1) a reaction of hematite with siderite (Burt, 1972); (2) hydrothermal fluids (Ohmoto, 2003); or (3) oxidation of organic matter, either through bacterial Fe(III) reduction (Konhauser et al., 2002; Kappler et al., 2005) or metamorphic reactions at temperatures above the threshold for microbial life (Perry et al., 1973; Morris, 1993). Specifically:

(1) Siderite reaction with hematite and subsequent formation of magnetite could explain the observations described here; i.e., magnetite overgrowths continuously along the con-
tact between hematite- and chert + siderite-rich laminae. The available evidence, however, suggests that the addition of Fe(II) from the reaction with siderite is favoured at relatively high temperatures and pressures. Even though nanometer-sized magnetite crystals have been reported from siderite at temperatures as low as 300 °C (Isambert et al., 2005), experimental determination of the reaction: FeCO$_{3(siderite)}$ + Fe$_2$O$_{3(hematite)}$ = Fe$_3$O$_{4(magnetite)}$ + CO$_2$ show the decomposition of reactants between pressures of 4 and 15 kbar and temperatures ranging from 440 to 650 °C (Koziol, 1999). Accordingly, the metamorphic grade of the Dales Gorge Member (see above) would have been insufficient to attain the siderite thermal decomposition and formation of magnetite. Additionally, in macroband #16 the δ^{56}Fe values for hematite and magnetite show neither intra- nor interlayer trends giving an overall uniform δ^{56}Fe of ca. −0.8‰, whereas siderite in contact with magnetite displays lighter δ^{56}Fe ca. −2.2‰ (Steinhofel, personal communication, 2008). Hence, we suggest that the reaction between hematite and siderite to form magnetite would not be viable to explain the observations described here.

(2) In a non-conservative system (i.e., open to Fe), the reactions between Fe(II)-rich hydrothermal fluids (<200 °C and H$_2$S poor) with earlier hematite could lead to magnetite formation (Ohmoto, 2003). In this regard, the REE and Nd isotope characteristics of some BIFs would indicate that the primary iron oxides formed by mixing of Fe(II)-bearing hydrothermal fluids with local seawater (Jacobsen and Pimentel-Klose, 1988; Derry and Jacobsen, 1990; Alibert and McCulloch, 1993; Bau and Möller, 1993). This model is based on volcanogenic massive sulfide deposits where the hydrothermal fluids produce massive transformations of the earlier phases near the vents (Ohmoto, 2003). However, in our samples, the conversion of hematite into magnetite is present as overgrows and it does not show any massive transformations. Furthermore, recent studies by Frost et al. (2007) and Johnson et al. (2008) have shown that despite the presence of intra-grain and intra-layer Fe isotopic variability in the 2.5 Gyr old Kuruman and Dales Gorge BIF, there is no evidence of iron exchange between consecutive layers in BIF or diagenetic/metamorphic resetting of Fe isotopes. In other words, it seems unlikely that the buried BIF layers were openly exposed to bottom seawater.

(3) Similar to the reaction between siderite and hematite, the addition of Fe(II) from the abiological reaction hematite + organic matter occurs at relatively high temperatures and pressures. Yet, abiological oxidation of organic carbon accompanied by CO$_2$ loss produces δ^{13}C values very different to those obtained in BIFs (see above). Instead, biogenic magnetite produced through reduction of Fe(III) oxyhydroxides by dissimilatory Fe(III)-reducing bacteria (DIR) is a well recognized pathway and is thought to have resulted in the accumulation of large amounts of extracellular magnetite (Fe$_3$O$_4$) through the reduction of Fe(III) oxides as the terminal electron acceptor for organic matter oxidation (Lovley, 1993). According to Johnson et al. (2008), the addition of Fe(II) with low δ^{56}Fe values to oxyhydroxides produces magnetite that has δ^{56}Fe < 0‰. Of all the three mechanism considered by the same authors (i.e., iron addition, excess aqueous iron and role of bacteria), partial Fe(III) oxide reduction by DIR would be the most likely means to produce low δ^{56}Fe values, typically between −0.5 and −2.5‰ lower than those of the initial ferric oxide/hydroxide (Johnson et al., 2008). Surprisingly, preliminary Fe isotopic work on our Dales Gorge samples shows that the magnetite has similar Fe isotopic values to its precursor hematite (Steinhofel, personal communication, 2008). This suggests that in the magnetite samples analyzed, there was complete conversion of the hematite where all the Fe(II) generated by DIR was consumed and no net change in

δ^{56}Fe values between the hematite and magnetite are produced (e.g., Johnson et al., 2008). Hence, the available evidence in this work – including petrologic data – supports a secondary origin for magnetite from hematite at relatively low temperatures, most likely through bacterial Fe(III) reduction.

Ankerite-ferroan dolomite and minor apatite are associated with Fe-oxide rich microbands. The former is preferentially concentrated when several Fe-oxide layers coalesce due to burial compaction, forming large crystals and distorting the primary microlamination. This feature clearly indicates the late-stage nature of the mineral, most likely representing a by-product of siderite dissolution and subsequent CO_2 release. Presumably, the thicker compressed Fe-oxides bands would act as a barrier to CO_2 diffusion, allowing the reaction of dissolved bicarbonate with cations (Ca, Mg and Fe) and the resulting formation of carbonate minerals. Apatite, which is uncommon, is mainly associated with Fe-oxide microbands. Assuming limited vertical phosphate remobilization during diagenesis, it is likely that the apatite precipitated either as two separate phases, preferentially with primary ferric hydroxides (now hematite) (Bjerrum and Canfield, 2002) or it was associated with the organic remains of planktonic bacteria that settled out to the seafloor (Konhauser et al., 2002).

4.2. Trace element geochemistry

The iron and trace element redox cycles, as evidenced by the enrichment in Fe-rich deposits (either detrital or chemical precipitates), are intimately interconnected in a wide range of trace metals. The factors that lead to these enrichments vary, and include a variety of processes occurring through the mobilization of particles/ions, during deposition and diagenesis (for excellent reviews see Chester, 2000; Burdige, 2006). In the following, we attempt to summarize the most abundant trace metals present in Dales Gorge BIF and their potential implications for the palaeo-ocean geochemistry.

4.2.1. Barium

In modern marine sediments, Ba is largely found in the form of barite (up to 70% of total Ba), but it is also associated with carbonates (~30%), aluminosilicates (300–2000 ppm) and Fe–Mn oxyhydroxides (1000–2000 ppm) (Dymond et al., 1992). The sources of Ba to the oceans are particulate biogenic sources, continental detritus, hydrothermal effluent, and diagentic remobilization/precipitation (Dymond et al., 1992). The strong correlation of Ba with organic carbon has led to the former's use as a proxy of ocean fertility (Goldberg and Arrhenius, 1958; Turekian and Tausch, 1964). For example, in the Kuruman Iron Formation in South Africa, a positive correlation between Ba and C_{org} has been recorded (Beukes et al., 1990, their Fig. 12C). However, the highest concentrations of Ba and C_{org} are found in nearshore shales, limestones and dolostones, whereas siderite-BIF and chert show the lowest Ba (<35 ppm) and C_{org} contents, causing some authors to suggest that low productivity existed in the water column above the BIF (Beukes et al., 1990).

In the Dales Gorge BIF, whole-rock analyses of macroband #15 show maximum Ba concentrations of 23 ppm, whereas macroband #16 reaches values as high as 35 ppm. Although significant in comparison with other trace metals (Table 2), Ba content is low when compared to that of modern sediments (see above). Furthermore, no barite has yet been documented in Dales Gorge BIF, wherein Ba is principally associated with hematite (~66 ppm) and magnetite (~24 ppm). A positive correlation between Ba and Fe ($r^2 = 0.47$) likely reflects the sorption capacity of Fe-oxides for Ba in contrast to carbonates which cannot retain this element, particularly

during redox mobilization of Fe-oxyhydroxides (e.g., Goldberg and Arrhenius, 1958).

4.2.2. Arsenic

Arsenic is present in extremely low concentrations in the upper continental crust, with an average of <2 ppm (Taylor and McLennan, 1985). Detrital sediments and ocean waters are also strongly depleted in As, but unmixed hydrothermal fluids can be enriched from 2 to 500 times seawater concentrations (mainly in the form of arsenate oxyanions ($HAsO_4^{2-}$ and $H_2AsO_4^-$)). The significant input of hydrothermal plume-fallout is evident in sulfide minerals and Fe- and Mn-rich sediments close to hydrothermal systems where high As concentrations have been recorded. Iron or Mn oxyhydroxide particles are well known scavengers of As and when suspended in plumes those elements rapidly adsorb As from the vent fluid as well as from ambient seawater (Feely et al., 1994). Furthermore, As is scavenged from seawater by organic matter. Once buried, the behaviour of As in sediment is controlled by pH and redox conditions. Arsenic's vertical distribution in pore-waters is strongly influenced by diagenetic processes—this is attributed to the combined effects of diagenetic remobilization under reducing conditions followed by upward migration and subsequent reabsorption onto Fe or Mn oxyhydroxides in the overlying suboxic/oxic layers. Experimental evidence shows that As is sequestered during the precipitation of Fe oxyhydroxides, in agreement with a sorption process onto the Fe oxyhydroxide precipitates, and its subsequent desorption and remobilization is due to changes in porewater pH (Le Guern et al., 2003). According to the same authors, the lack of correlation between the kinetics of Ca and As evolution and the low concentration of As in calcite (11 ppm) indicates that calcite precipitation plays a minor role in As trapping.

Based on the very low As concentrations in bulk analyses (<1 ppm) and Fe-oxides (<13 ppm) from the Dales Gorge Member (Tables 1 and 2), the following geochemical scenario is proposed. The settling of initial ferrihydrite particles (formed in the photic zone of the oceans) was accompanied by scavenging of As through sorption and/or co-precipitation reactions. Once precipitated and subsequently buried in the sediment to the zone of active bacterial Fe(III) reduction, As is released into the pore-water. Some As may then become incorporated into siderite (also formed via ferric iron reduction), explaining the high concentrations of As (~62 ppm) in that mineral phase. In this model, other chemical reactions would also have influenced As mobility, including competition of Si with As for sorption sites on ferric hydroxide particles (Swedlund and Webster, 1999).

4.2.3. Chromium

Similar to other transition metals, Cr can occur in several oxidation states, with Cr(III) and Cr(IV) being the two most stable. While the latter is very mobile in natural environments, Cr(III) is characterized by a low aqueous solubility. Redox reactions, either biotic or abiotic, are the main factors controlling Cr transport in the natural environment. Biotic reduction is mediated by chemoheterotrophic bacteria that use Cr(IV) as an electron acceptor, while abiotic pathways include reductants such as Fe(II). In this regard, Fe(II) is ubiquitous in many silicates, carbonates and oxides, while the bacterial reduction of Fe(III) provides a source of dissolved Fe(II). In the water column, Cr(VI) is present in anionic forms, mainly as chromate ($CrO4^{2-}$) or bichromate ($HCrO_4^-$), which are generally soluble over a wide pH. Similar to other chemical species, such as V, As and P, these anionic species can be scavenged through adsorption onto the surfaces of ferric oxyhydroxide particles (Chen and Hao, 1996). In this regard, those anions may similarly affect the sorptive properties of Cr.

Samples from Dales Gorge Member show relatively significant concentrations of Cr in hematite (~25 ppm), suggesting adsorption

of Cr onto ferric oxyhydroxides. Magnetite and siderite are also significant Fe(II) containing minerals in Dales Gorge BIF and show Cr average contents of ~20 and ~16 ppm, respectively. In this case, such Cr concentrations can be explained by the potential of the minerals to reduce and precipitate Cr(VI) at Fe(II) sites, most likely during diagenesis (Deng et al., 1996; White and Peterson, 1996; Kendelewicz et al., 2000; Alowitz and Scherer, 2002).

4.2.4. Zinc

In modern marine sediments, crust-derived lithogenous material and, to a lesser degree, hydrothermal fluxes contribute largely to the total Zn content of deep-sea sediments (Chester, 2000). Zinc is principally present in seawater as hydroxide and carbonate complexes and its concentration in solution is controlled by adsorptive interactions with suspended particles, including aluminium silicates, organic complexes and ferric oxyhydroxides (Millero, 1996; Benjamin and Leckie, 1981; Zachara et al., 1988).

In the Dales Gorge BIF macrobands #15 and #16, Zn is preferentially concentrated in ferran-talc (~44 ppm) and siderite (~25 ppm), with minor amounts in magnetite, hematite and ankerite-ferroan dolomite (<17 ppm). Zn along with Cd, Cu, Co, Pb, Ni are chalcophile elements and as such their concentrations are strongly depleted in anoxic waters due to the precipitation of respective solid sulfides. However, the anomalously low sulfate model proposed by Canfield (1998) for late Archean–early Paleoproterozoic oceans implies that sulfide was not a likely sink for Zn during deposition of the Dales Gorge BIF. All these observations suggest that the precipitation of Zn in the Dales Gorge BIF was largely associated with ferran-talc and siderite. Furthermore, the ability of Zn to partition into ferric oxyhydroxides indicates that it was also brought to the seafloor with the sedimenting ferrihydrite particles, and once buried, subjected to remobilization via Fe(III) reduction, with subsequent re-sorption onto ferrous-iron containing minerals.

4.2.5. Strontium

Given that the residence time for Sr in the ocean is long (4.9×10^6 year; Chester, 2000), seawater integrates the flux of Sr from various sources. As a consequence of continental crust weathering, river run-off is the dominant input of dissolved Sr (~75%) to seawater. Other fluxes result from the diffusion of Sr from the porewaters of marine sediments, principally carbonate-rich, and from interaction between seawater and basalt during high-temperature hydrothermal activity at spreading centers and vents. Strontium shows both enrichment and depletion in the hydrothermal fluids relative to seawater: its average concentration in hydrothermal solutions reaches 82 μmol kg^{-1}, but in fast spreading-ridges can be as high as 253 μmol kg^{-1} (Chester, 2000). A number of studies have demonstrated the sorption of Sr to Fe- and Mn-oxyhydroxides (e.g., Trivedi and Axe, 1999), and in this regard, it has been suggested that Sr does not behave conservatively in the water column since it is removed by sedimentation of Fe-Mn oxyhydroxide particulates. Subsequent Fe(III) reduction then potentially releases the trapped Sr to sediment pore-waters.

A similar pattern of sorption and remobilization can be used to explain the measurements of Sr in the Dales Gorge BIF macrobands #15 and #16, where Sr is found at concentrations of not only 22 ppm in hematite, but also 10 ppm in magnetite. This would suggest that Sr was incorporated into ferrihydrite as it formed in the photic zone, and subsequently trapped by secondary mineral phases during diagenesis (i.e., magnetite and most probably carbonates as shown by the positive correlation between Sr and Ca $r^2 = 0.57$).

4.3. Implications for the source of the Dales Gorge BIF

The geochemistry of fine-grained siliciclastic rocks has been successfully applied in the study of provenance, source area weathering conditions, and evolution of continental crust through time (e.g. Taylor and McLennan, 1985; McLennan and Taylor, 1991). Similarly, geochemical studies of marine precipitates, including cherts and BIFs, have been used as proxies to identify secular trends in Precambrian ocean chemistry (Klein, 2005; Maliva et al., 2005; Ohmoto et al., 2006). However, radically different views have been proposed for the geochemistry and isotope composition of the Precambrian oceans varying between continent-dominated (e.g., Miller and O'Nions, 1985) and hydrothermal-dominated (e.g., Derry and Jacobsen, 1990) models.

Much, if not most, of the evidence suggests that chemical components of BIFs were sourced from hydrothermal systems (Klein, 2005). With respect to the Dales Gorge BIF, a study on Ge/Si ratios from the same core studied herein, however, indicates that the sources of Si and Fe were decoupled during sedimentation, with Si being dominantly derived from weathering of continental landmass and Fe having a hydrothermal origin (Hamade et al., 2003). Supporting this hypothesis and based on REE content, evidence of irregular dominance of continental and hydrothermal input on the Dales Gorge Member has been presented by Morris (1993), but according to Klein and Beukes (1989; their Fig. 19b) the influence of hydrothermal activity as a source of these deposits is clear. Thus, depleted REE patterns (especially light REE) with positive Eu anomalies and Nd isotopic signatures are considered to be conclusive proof of hydrothermal influence (Dymek and Klein, 1988; Jacobsen and Pimentel-Klose, 1988; Klein and Beukes, 1989; Beukes and Klein, 1990; Derry and Jacobsen, 1990; Bau and Möller, 1993; Klein, 2005). The geochemical arguments have recently been augmented by sedimentological evidence, with Krapež et al. (2003) and Pickard et al. (2004) suggesting that the Fe oxide macrobands initially were precipitated as iron-rich hydrothermal muds, deposited on the flanks of submarine volcanoes under the action of density currents. By contrast, a petrographic study of the conglomerates present in the Dales Gorge Member has shown that the clastic detritus – black chert and limestone – were predominantly derived from erosion of a carbonate shelf (Krapež et al., 2003).

Our study has contributed to the database on the Dales Gorge BIF by providing a detailed mineralogical and geochemical framework with which to test the previous depositional models. Specifically, a comparison can be made of major and trace element geochemistry of S and BIF macrobands as well as related lithologies with potential source rocks as a means of defining the provenance, i.e., whether they were derived from the continent, basin floor or hydrothermal vents. In order to identify the composition of a sediment source area, binary plots of immobile element pairs can be used. The most useful diagrams involve combinations of the elements such as Al, Ti and Zr, but REE, Th, Sc and the HFSE (high field strength elements) are also helpful (e.g., McLennan et al., 1993). Lithological variations in the source area can be effectively monitored by plotting ratios such as Al_2O_3/TiO_2 or Zr/TiO_2.

Available data from the Fortescue and Hamersley groups for Al_2O_3 and TiO_2 is plotted in Fig. 11. Al_2O_3/TiO_2 ratios are generally between 10 and 20 in Fortescue and Weeli Wolli basalts, about 20 in S macrobands, and – although more disperse – <20 in BIF macrobands. Thus, a nearly continuous trend from basalts to BIF macrobands is observed. A similar trend is displayed when Zr vs. TiO_2 values are plotted (Fig. 12). Collectively, these figures demonstrate that the Dales Gorge S bands, having relatively high Al_2O_3 and positive correlations with TiO_2 and Zr, were derived from detrital and volcaniclastic sources, similar to the earlier findings of Barley et al. (1997) and Krapež et al. (2003). With regards to the Fe oxide macrobands, when the relative contribution of terrigenous (Al, Fe, Ti) and hydrothermal/hydrogenous (Fe, Mn) components in Dales Gorge BIF are plotted, they fall close to the modern chemical sediment end, suggesting a marine hydrothermal source for the Fe (Fig. 13). Therefore, a continuous gradation from the source rocks
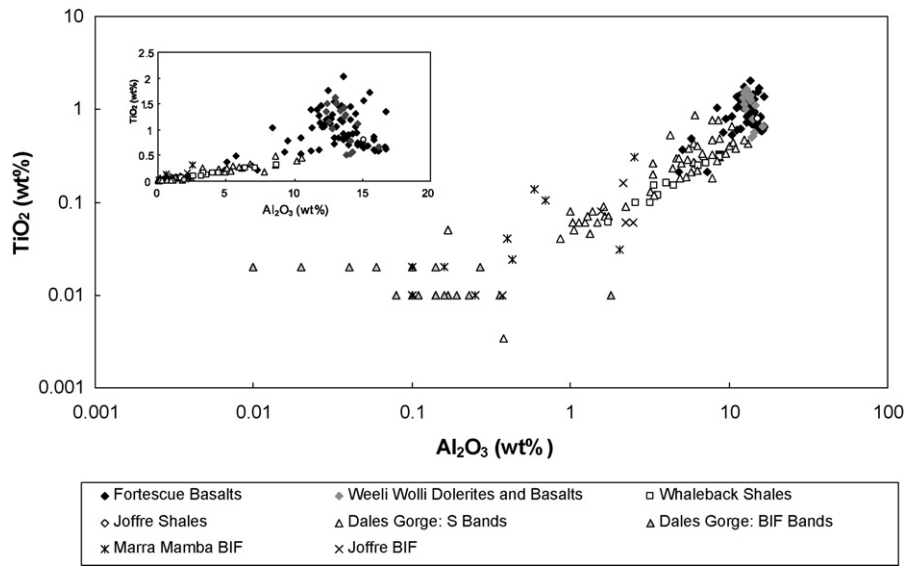
Fig. 11. Al_2O_3 vs. TiO_2 diagram showing BIF and S macrobands from the Dales Gorge Member and Weeli Wolli-Fortescue basalts. Other BIFs and associated shales have been included for comparison (*sources*: Ewers and Morris, 1981; Klein and Gole, 1981; McConchie, 1987; Nelson et al., 1992; Alibert and McCulloch, 1993; Arndt et al., 2001; Pickard, 2003; Webb et al., 2003; this study).

to mixed chemical–detrital and pure chemical sediments supports the hypothesis of two decoupled sources during the sedimentation of BIF and S macrobands.

In modern marine environments (e.g., the Red Sea), submarine hydrothermal plumes discharge high concentrations of dissolved Fe(II), which is spontaneously oxidized upon exposure with oxygenated seawater, and the resulting Fe(III) oxides precipitate in proximal sediments (Gurvich, 2005). Likewise, the net flux of iron to the oceans via river run-off is severely limited under oxygenic conditions (Chester, 2000). During the early Precambrian, however, more vigorous hydrothermal activity along with a long-time persistence of Fe(II) in solution under anoxic conditions suggest that hydrothermal fluxes could have had a major impact on the global Fe circulation in the oceans (e.g., Derry and Jacobsen, 1990).

Similarly, anoxic weathering processes would have facilitated the mobilization of Fe(II), as demonstrated by the loss of Fe from pre-2.2 Ga paleosols (e.g., Rye and Holland, 2000), and its transport to the oceans (Cloud, 1968; Lascelles, 2007). In addition to REEs and Nd isotopic composition (see below), the low concentrations of lithogenous elements (e.g., Al_2O_3, TiO_2, and K_2O) in the Dales Gorge BIF macrobands challenge a major continental source of Fe in detrital minerals as proposed by Drever (1974) and Holland (1984). This, however, does not rule out the possibility of a continental source of dissolved Fe(II) as a fraction of the total Fe.

In the plots discussed above, which are based on immobile elements, it is assumed that sedimentary rocks can be treated by relating them along the alteration lines to the proper parent rocks (e.g., Amajor, 1987). During subaerial weathering, however,
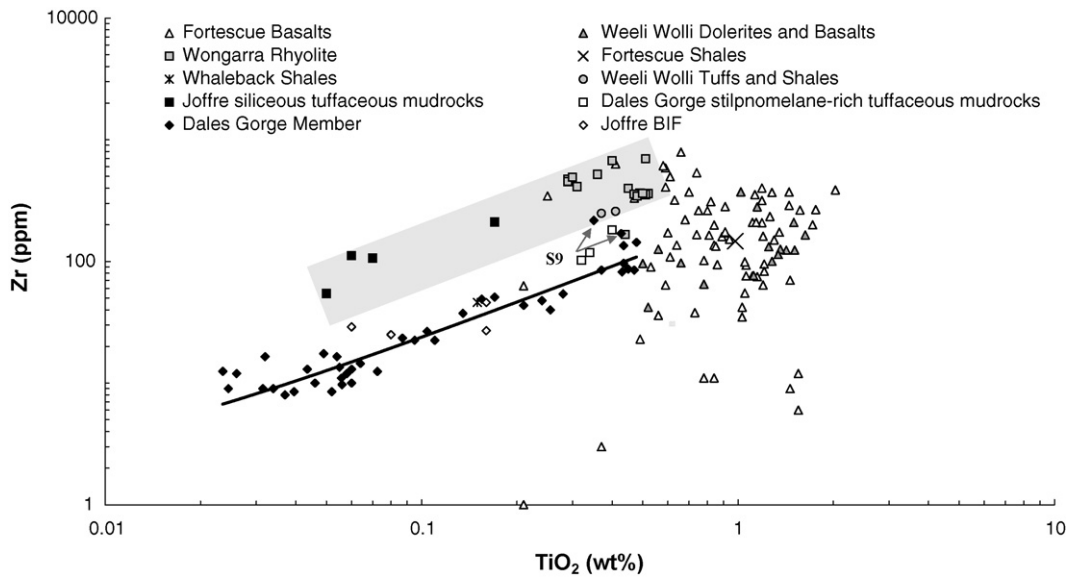

Fig. 12. Zr vs. TiO_2 abundances for selected sedimentary and volcanic rocks from the Fortescue and Hamersley groups. Joffre Member siliceous tuffaceous mudrocks have similar ratios to those of the Woongarra Rhyolite defining an 'acidic alteration trend' (grey area). The vast majority of the Dales Gorge Member samples delineate a linear trend consistent with a basic dominated source. Some few points, which correspond to macroband S9 and stilpnomelane-rich tuffaceous mudrocks, have ratios consistent with mixing of two provenances (*sources*: Ewers and Morris, 1981; Nelson et al., 1992; Alibert and McCulloch, 1993; Barley et al., 1997; Arndt et al., 2001; Pickard, 2003; this study).
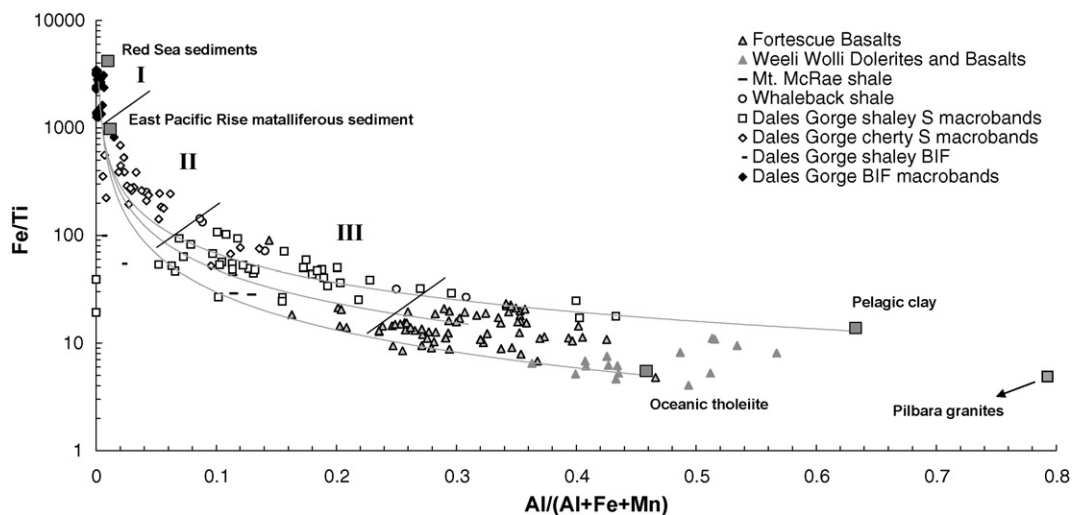
Fig. 13. Plot showing the composition of Dales Gorge macrobands, associated shales, and potential parental end member rocks in terms of Fe, Ti, Mn and Al (modified from Boström, 1973; Barrett, 1981). Curves represent ideal mixing between metalliferous sediment and oceanic basalt (lower curve) and metalliferous sediment with terrigenous sediment (upper curve). Likewise, a curve representing mixing between Dales Gorge BIF and Weeli Wolli-Fortescue basalts (middle curve) is showed. BIF macrobands overlap the composition of metalliferous hydrothermal sediments in the zone I, cherty S macrobands show a minimum hydrothermal contribution in zone II, shaley S macrobands and associated shales display a transition between BIF-S macrobands and Weeli Wolli-Fortescue basalts (zone III). Note that no shales are recorded between basalts and granites (pelagic and terrigenous sediments domain) (*sources*: Ewers and Morris, 1981; Nelson et al., 1992; Alibert and McCulloch, 1993; Bickle et al., 1993; Barley and Pickard, 1999; Arndt et al., 2001; Pickard, 2003; Webb et al., 2003; this study).

progressive enrichment/depletion of certain elements can be produced, making the relationship of parent rocks to sediment less clear. In order to compensate for this, one accepted approach is to quantify the degree of source weathering through the use of a chemical index of alteration (CIA; Nesbitt and Young, 1982; Fedo et al., 1995) for possible cratonic sources for the S macrobands, including komatiites, basalts, granites and rhyolites, and the thick volcanic pile of the Fortescue Group (Fig. 14). On the A–CN–K diagram, none of the samples follow the expected weathering trend of

(ultra)mafic (arrow A_1) or felsic rocks (arrow A_2). Shaley and cherty S macrobands, as well as various selected shales, plot along the A–K line (right side of the ternary plot), clearly showing K enrichment as a result of post-depositional K-metasomatism (arrow B). In other words, K is added later during burial or metamorphism, which explains the offset respect to the typical weathering trends.

The K addition likely comes from the conversion of Al-rich clays to those potassic in composition, such as illite or muscovite (Nesbitt and Young, 1989). Indeed, these mineral phases and their chemical
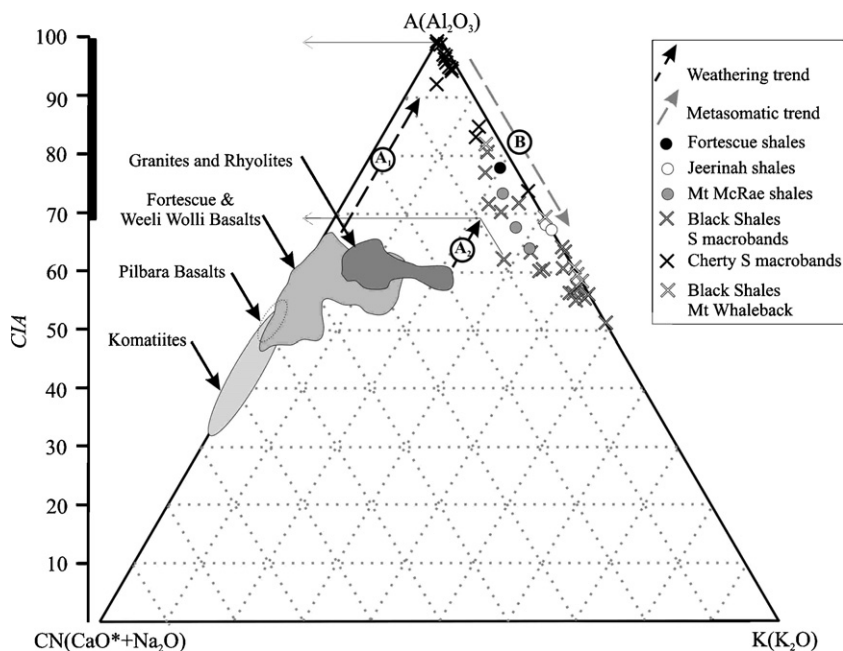

Fig. 14. Al_2O_3–$(CaO^* + Na_2O)$–K_2O (A–CN–K) diagram for Dales Gorge S macrobands and associated shales from the Hamersley and Fortescue groups (compositions in molecular proportions; CaO^* represents CaO of the silicate fraction only). The black dashed arrows show the predicted weathering trend of ultramafic (A_1) and felsic rocks (A_2) that these rocks must have followed before addition of K (B). The data points define a linear trend along the A–K axis. This line intersects the A–CN axis at *ca.* 69 for felsic and *ca.* 98 for (ultra)mafic rocks (horizontal arrows). These values represent the possible range of premetasomatized chemical index of alteration (CIA) (*sources*: Nesbitt et al., 1979; Ewers and Morris, 1981; McLennan et al., 1983; Nisbet et al., 1987; Nelson et al., 1992; Alibert and McCulloch, 1993; Bickle et al., 1993; Ohta et al., 1996; Barley et al., 1997, 2000; Barley and Pickard, 1999; Arndt et al., 2001; Pickard, 2003; Webb et al., 2003; Smithies et al., 2007; this study).
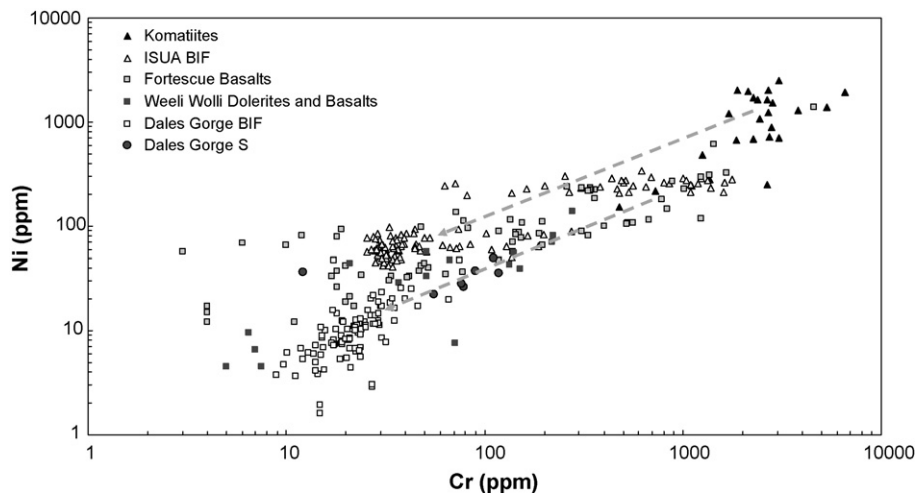
Fig. 15. Plot of Ni against Cr content for iron oxides present in Dales Gorge BIF macrobands #15 and #16 and whole-rock analyses from the Weeli Wolli and Fortescue basalts (Nelson et al., 1992; Arndt et al., 2001; Pickard, 2003). Data from ISUA BIF and komatiites is plotted for comparison (komatiites values taken from Nesbitt et al., 1979; Nisbet et al., 1987; Barley et al., 2000). Having a similar trend to that depicted between Dales Gorge and Weeli Wolli-Fortescue samples (lowermost arrow), BIF from ISUA shows higher Ni–Cr values (see text for explanation).

transformations have been extensively recorded in the Dales Gorge Member as a consequence of pervasive and localized alteration during diagenesis and low-grade metamorphism (Webb et al., 2003). More recently, Ohmoto et al. (2006) suggested a decrease in the K_2O content in the McRae shales, ranging from ~4 to <1 wt%, as a consequence of the hydrothermal activity in the proximity of the feeder zones. Such depletion in the shales would help explain the origin and relative enrichment of K in other areas. Based on the predicted weathering trend for felsic and (ultra)mafic rocks previous to K-metasomatism, the CIA values for shaley and cherty S macrobands, as well as shales from the Mt. McRae Formation, can be attained by locating the samples back along the A–K join to the intersection with the proper weathering trends. Therefore, the CIA values range from 69 to 98, which indicate deep chemical weathering of the source area and suggest that the parent rocks must be exposed to subaerial erosion.

The average Ni/Cr ratio of the Dales Gorge Member defines a linear trend with that of the underlying and overlying mafic igneous rocks (Fig. 15), providing additional evidence of a mafic-dominated source, as suggested here (see also Fig. 16). A similar relationship is seen, for example, when komatiites and BIF from the ISUA greenstone belt are plotted (Konhauser et al., 2009). The latter, however, displays higher Ni–Cr values due to a more ultramafic component. In fact, high abundances of Ni (and Cr) have also been noted in several Archean clastic sedimentary rocks, and have generally been explained by the presence of an ultramafic source (e.g., McLennan et al., 1983; Fedo et al., 1996). Average compositions of post-Archean shales and greywackes define a progressive decrease in Ni concentration through time, a pattern best explained by compositional changes from an ultramafic to felsic upper continental crust (e.g., Condie, 1993). Comparison of the mean concentration of Ni in major BIF types through time shows a similar trend (see below). Samples of Algoma-type BIF of early Archean age (3.8 Ga) from Isua, west Greenland, have Ni values as high as ~58 ppm (Dymek and Klein, 1988). The mean content for samples from Lake Superior-Type BIF from Kuruman–Griquatown sequence (2.3 Ga), South Africa, drops to ~31 ppm (Beukes and Klein, 1990), and further to ~10 ppm in the 0.75 Ga Rapitan Iron Formation in Canada (Klein and Beukes, 1993).

The presence of conspicuous positive Eu anomalies and Nd isotopic signatures in Archean and some Paleoproterozoic BIFs has been attributed to hydrothermal signatures (Klein, 2005 and references therein). Hydrothermal activity along spreading ridges and vents induces hydration of the Mg-olivine and orthopyrox-
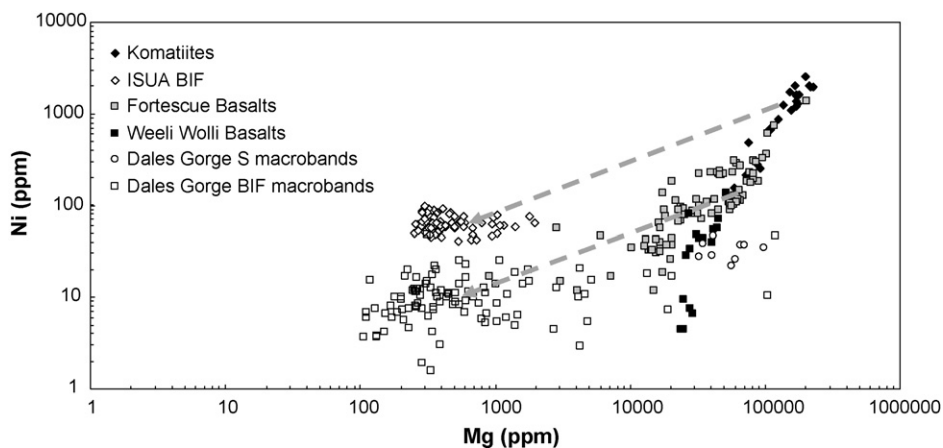

Fig. 16. Plot Ni + Cr against MgO showing the colinearity between Weeli Wolli-Fortescue basalts and iron oxides from Dales Gorge Member macrobands #15 and #16 (lowermost arrow). Similarly to Fig. 14, a comparable trend between komatiites and BIF form ISUA is observed. Note that S macrobands overlap the basalt field (sources for basalts and komatiites as in Fig. 14).
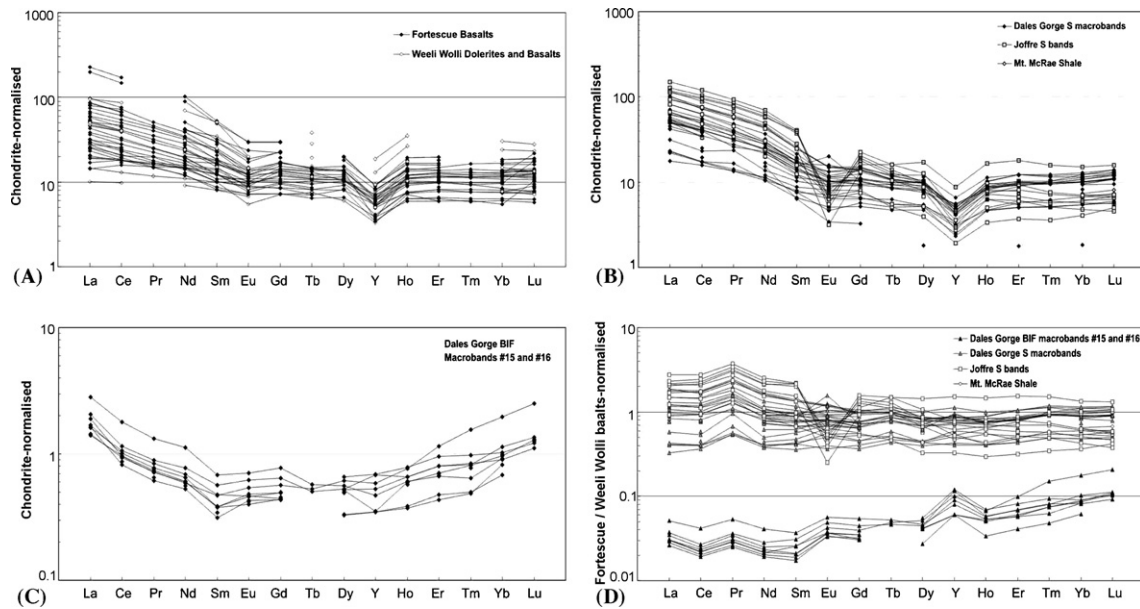
Fig. 17. (A) Chondrite-normalised REE + Y diagram of Fortescue basalts (source as in Fig. 14). (B) Chondrite-normalised REE diagram of Mt. McRae and Joffre shales and Dales Gorge S macrobands (source: Alibert and McCulloch, 1993). Despite no Pr, Tb, Y, Ho and Tm values were measured, notice the low overall abundance of LREEs and the flat pattern defined by HREEs. (C) Chondrite-normalised REE + Y diagram of Dales Gorge BIF macrobands #15 and #16. (D) Fortescue-Weeli Wolli normalised REE + Y diagram comparing Mt. McRae and Joffre shales, Dales Gorge BIF and S macrobands (source: Nelson et al., 1992; Alibert and McCulloch, 1993; Arndt et al., 2001; Pickard, 2003; this study).

ene minerals in the oceanic crust (i.e., serpentinization). This leads to the release of transition metals (including Ni and Fe) in variable proportion depending on the fO_2 and fS_2. However, the newly formed serpentine minerals (e.g., brucite) and Fe-oxides (magnetite, awaruite, etc.) can accommodate, along with sulfides, considerable amounts of Ni and thus, its release would be limited. Therefore, we envisage that, at least, a substantial part of the Ni and Cr present in Dales Gorge BIF derive from the Fortescue and/or Weeli Wolli basalts (see below).

A prevailing mafic provenance is also indicated by REE compositions. A comparison between the chondrite-normalized REE patterns from shales and BIFs with rock analyses of granites, rhyolites, and komatiites from the Pilbara Craton, and Weeli Wolli and Fortescue basalts, suggests that the shales and S macrobands were largely derived from the latter lithologies (Fig. 17A). This suggestion is also based on the low overall abundance of LREEs and by the flat pattern of HREEs (Fig. 17B). It is noteworthy that the Mt. McRae shale, and some of the samples from the Joffre Member, display a negative Eu anomaly (Eu/Eu* = 0.8–0.9), although this observation is based on few samples and no Zr values are available to account for possible zircons, or other heavy mineral contaminants that may produce such anomaly (Taylor and McLennan, 1985). Nonetheless, the observed REE patterns have PAAS characteristics and thus, the Eu/Eu* ratios probably reflect the source rock type. For example, shales from the underlying Fortescue Group, which clearly derived from the Pilbara Craton, show comparable REE patterns to those of the Mt. McRae and Joffre Member (see Taylor and McLennan, 1985; their Fig. 8.6). While the negative Eu anomalies might indicate an additional granitic source (e.g., Taylor and McLennan, 1985; Condie, 1993), Fortescue shales have high Ni and Cr contents clearly indicating an ultramafic source (Taylor and McLennan, 1985). Similarly, a suitable source for the Hamersley fine-grained sedimentary rocks would be represented by the Weeli Wolli and Fortescue basalts, with comparatively low Ni and Cr contents.

A transition from continental- to intrabasinal-dominated source has been proposed by Alibert and McCulloch (1993). Based on Nd isotopic compositions, the authors suggested a cratonic source for

the lower Fortescue shales, an upper Fortescue Group source for the lower Hamersley Group and a submarine hydrothermal source for the Dales Gorge and Joffre BIFs. The shaley bands (S macrobands), however, exhibit attenuated or inexistent Eu anomalies, which account for a more dominating mafic source. Conversely, BIF macrobands record a remarkable V-shaped pattern (Fig. 17C) and display a positive Eu anomaly, which has been traditionally linked to hydrothermal activity (e.g., Klein, 2005). The REE pattern can be interpreted as a result from the mixing of two end member source rocks or by the fact that iron oxyhydroxides preferentially adsorb HREE (Leleyter et al., 1999). The last interpretation is supported by strong relationships between Fe and HREE (not shown). When comparing REE patterns of BIF macrobands and shales (Mt. McRae, S macrobands and Joffre) with Weeli Wolli and Fortescue basalts, REE contents in shales, and particularly in BIF, are somewhat lower (Fig. 17A–C). Normalizing shales using Weeli Wolli and Fortescue basalt analyses illustrates a slight and homogenous depletion of all REE (Fig. 17D), which is most likely due to submarine weathering of basaltic rocks (Frey et al., 1974; Nesbitt, 1979). BIF macrobands show a pronounced enrichment of the HREE relative to the LREE, which mimics the distribution pattern of REE in the marine environment (see Ruhlin and Owen, 1986).

4.4. Constraints on the source of BIFs

S macrobands mainly comprise volcanogenic (mafic and contemporaneous ash) and carbonate muds, as well as coarser-grained clastic limestones and chert clasts. The sedimentological and stratigraphical data show evidence of episodic density flows within S macrobands, interpreted as turbidites, while the absence of wave modification and coarse-grained deposits, in addition to the presence of hemipelagites, indicates a deep water (basin-floor) depositional setting (Pickard et al., 2004). BIF macrobands are largely interpreted to have been hydrothermal muds, composed of iron-rich smectite and particles of iron oxyhydroxide and siderite, which would include direct deposits of hydrothermal vents and hydrothermal alteration products of basaltic debris deposited on the flanks of submarine volcanoes and resedimented by density
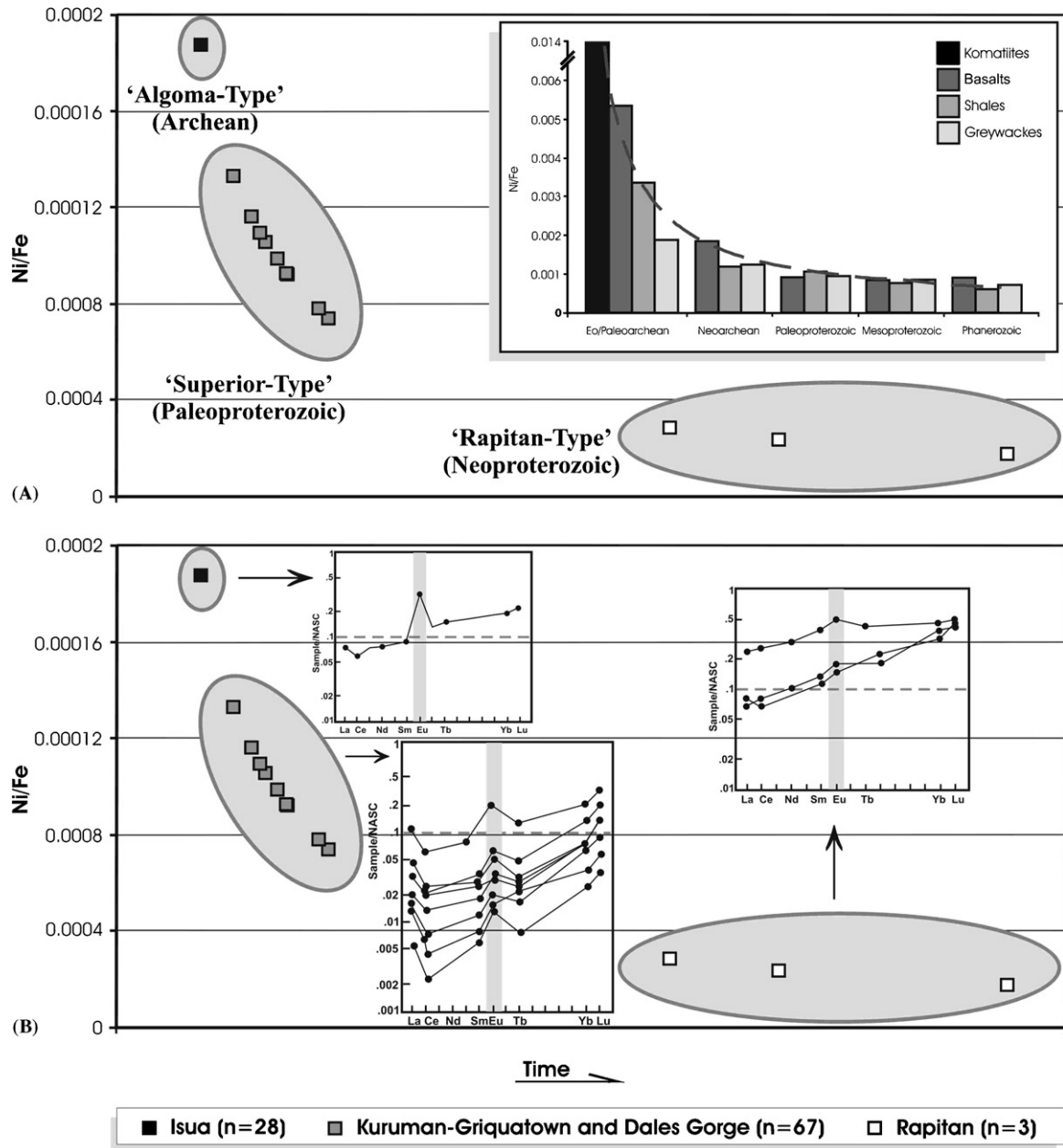
Fig. 18. Two opposite scenarios for element supply to BIFs: 'weathering-sourced' and 'hydrothermal-sourced'. (A) and (B) display Ni/Fe ratios for Algoma-, Lake Superior-, and Rapitan-type BIFs through time. Concentration of Ni and Fe taken from: Dymek and Klein (1988), Beukes and Klein (1990), Klein and Beukes (1993) and this study. Kuruman-Griquatown samples include: oxide, siderite, peloidal, banded, and rhythmite facies. Rapitan samples include: nodular, banded, and arenite facies. Inset in (A) shows the Ni/Fe ratios through time for (ultra)mafic rocks and clastics (*sources*: Nesbitt et al., 1979; McLennan et al., 1983; Gibbs et al., 1986; Nisbet et al., 1987; Alibert and McCulloch, 1993; Condie, 1993; Barley et al., 2000). Insets in (B) shows the REE patterns for the major types of BIFs through time (source: Klein, 2005 and references therein). Depleted rare earth element patterns (especially LREE) along with the presence of conspicuous positive Eu anomalies in Archean BIFs have been attributed to hydrothermal signatures, whereas the hydrothermal sediments deposited away from vents are characterized by non-existent or attenuated positive Eu concentrations, such as the case of Neoproterozoic BIFs (Klein, 2005).

currents (Krapež et al., 2003). Hence, the compositional differences between S and BIF macrobands are directly attributed to shelf and intrabasinal sediment sources, respectively (Pickard et al., 2004).

With rare exceptions (e.g., S9 macroband; Fig. 12), the geochemical data presented here supports a dominantly mafic provenance for the S macrobands. Two possible sources are put forward: (i) Fortescue Basalts, and (ii) Weeli Wolli Basalts. Based on major, trace and REE elements, both basalts are geochemically identical and thus, it is difficult to place constraints on the dominant source at the time of deposition. In this regard, neodymium isotopic studies of the Jerrinah and Marra Mamba BIF and shales

have ε_{Nd} values between −1 and 0, thought to reflect the composition of the Fortescue Basalts (Alibert and McCulloch, 1993). Up section, the Dales Gorge and Joffre BIF display more positive ε_{Nd} values: +1 ± 0.5. The latter, according to the same authors, show the influence of a hydrothermal component in a similar proportion relative to the continental-derived component. Indeed, the increased abundance of tuffaceous mudrocks (with younger zircons) and the evolution from mafic- to acidic-derived tuffs from the Dales Gorge BIF to Joffre BIF account for a pulse of enhanced igneous and hydrothermal activity during the deposition of the Brockman Iron Formation (Pickard, 2002). Hence, the lithological and isotopic evolution observed between the Fortescue Basalts and Weeli

Wolli Formation-Woongarra Rhyolite show an increasing source of younger juvenile mafic (and acidic) material.

Irrespective of the mechanism, BIF have been traditionally considered a record of alternating precipitation of iron minerals and silica from seawater (Klein, 2005). Conversely, Krapež et al. (2003) postulated that the precursor sediments to BIF macrobands, in contrast to S macrobands, originated from iron-rich hydrothermal muds deposited on the flanks of submarine volcanoes. Several lines of evidence, including REE, fluid inclusions, O and Nd isotope signatures, show that the primary iron oxides of some BIFs formed by mixing Fe(II)-bearing hydrothermal fluids with bulk seawater (Klein, 2005; Ohmoto et al., 2006). A recent study on the Hamersley Basin sediments suggests that hydrothermal processes contributed to the distribution of multiple sulfur isotopes in pyrite of carbonate-bearing BIF layers and appears to have a different or additional sulfur source to that of the Whaleback Shale (Partridge et al., 2008). Even though this is in agreement with a major hydrothermal contribution to BIF macrobands, it also recognizes, as already mentioned, a different source for shales and consequently, for S macrobands. Similarly, studies on Ge/Si ratios indicate that the sources of Si and Fe were decoupled during sedimentation, with Si being dominantly derived from weathering of continental landmass and Fe having a hydrothermal origin (Hamade et al., 2003). Supporting this hypothesis and based on REE patterns, evidence of irregular dominance of continental and hydrothermal input on the Dales Gorge BIF has also been presented (Morris, 1993). Indeed, when analyzing geochemical patterns of the most likely parental rocks (i.e., Fortescue and Weeli Wolli Basalts) with BIF and S macrobands continuous trends can be observed (Figs. 11–13, 15 and 16). This indicates that at least part of the precursor material of BIF macrobands was sourced from the same material from which the S macrobands stemmed. This contribution could either be supplied as very fine particles or most likely, through dissolved species. This dual source is supported by neodymium isotopic data, which suggests a hydrothermal component of $50 \pm 10\%$ for the Dales Gorge and Joffre BIFs (Alibert and McCulloch, 1993).

Iron is the most significant constituent of BIF and under CO_2-rich and anoxic or poorly oxygenated atmosphere the enhanced chemical weathering, as suggested by the loss of Fe from >2.2 Ga paleosols (Rye and Holland, 2000), would have contributed significantly to the total Fe budget to the oceans. Along with Fe, other chemical species might have undergone the same fate. A good example is Ni, which is ubiquitous in (ultra)mafic rocks, depleted in >2.2 Ga paleosols (Rye and Holland, 2000), and generally scavenged and absorbed on iron oxyhydroxides in seawater (Chester, 2000). Similar to sedimentary clastic rocks, a progressive decrease in Ni concentration through time in BIFs, can be best explained by a compositional change from an ultramafic to a more felsic upper continental crust (cf. Condie, 1993; Konhauser et al., 2009). Even though, this can also be explained as a result of the progressive decrease in the hydrothermal activity, the likely influence of weathering cannot be ignored. Hence, using the available evidence two scenarios are put forward to explain the source of Fe and Ni, namely: (i) processes involving low-temperature weathering of the continental and ocean basement rocks, mainly (ultra)mafics; and (ii) high temperature water–rock reactions associated with hydrothermal activity at spreading ridge centers or seamounts (Fig. 18). In the first case ('weathering-sourced' model), the progressive decrease in Ni content as a result of a compositional change of the upper continental crust is most likely a direct consequence of cooling of the mantle with time (e.g., Condie, 1993; Berry et al., 2008). The relationship between high heat flow and Ni contents during the early Precambrian is corroborated in komatiites and basalts, where there also appears to be a systematic variation in the composition through time (Arndt, 1991). Hence, weathering of continents (and oceanic plateaus) will contribute clastic sediments and dissolved

solute composition that reflects the parent rocks. With respect to 'hydrothermal-sourced' model, the transition from Archean to Neoproterozoic BIFs, which become more 'seawater-like', is also accompanied by a diminishing Ni content. Modern hydrothermal deposits show high values of Ni (Chester, 2000), in agreement with the alleged affinity of Ni and BIFs with hydrothermal influence. Therefore, this consistently positive correlation between Eu and Ni concentrations suggests that Ni contents in BIFs is a function of the hydrothermal activity, and thus, could reflect the derivation of these elements throughout the leaching from mafic or ultramafic rock sources. In either case, the influence of the compositional change of the upper continental crust played a major role in the chemical compositions of BIFs. To what extent these elements, and other potential species (e.g., Cr), were sourced from hydrothermal fluids and surficial weathering remains unresolved.

5. Conclusions

Petrological and geochemical analysis of the Dales Gorge Member has led to the following conclusions:

1. Primary microbands are laterally continuous and display a regular thickness, commonly between 0.5 and 8 mm, defined by an alternation of "iron-rich" and chert-rich microlaminae ("iron-poor" microbands). Cyclic intercalations of (i) siderite-ferroan-talc-chert, with minor hematite, and (ii) almost pure chert were identified within chert-rich microbands. The contact between the two types of microlayers within the "iron-poor" microbands is gradational but passes abruptly into "iron-rich" microbands, which do not show any internal alternation. Whether this microbanding reflects: direct precipitation from the water column, redeposited chemical sediments (turbidites) or a diagenetic feature still remains uncertain.

2. Iron-rich microbands consisting of hematite often show magnetite overgrowths near the top and at the base of the layers. Hematite is texturally variable displaying massive anhedral aggregates and coarse xenomorphic crystals, and rarely platy habits. Magnetite normally shows subhedral to euhedral crystals. Associated with iron-rich bands are crystals of apatite and ferroan dolomite-ankerite. Chert-rich microbands contain mainly siderite, ferroan-talc and quartz, however, isolated crystals of hematite are also present.

3. As primary precipitates, hydrous amorphous silica would have crystallized as pure chert and cationic silica gels as siderite and possibly greenalite, the latter entirely transformed into ferroan-talc. In addition, ferroan-talc is arguably a reaction product of siderite and chert. BIF macroband #15 show a more advanced stage of transformation (dissolution) than that of macroband #16, which is also accompanied by an increase of ferroan-talc and a diminished siderite content. The initial precipitate to hematite is likely to have been ferrihydrite. There is no evidence of magnetite as a primary precipitate. Rather, it tends to occur as overgrowths on hematite and its origin is explained by the addition of Fe(II), derived from deep marine anoxic waters, to the iron (hydr)oxide layers. Early diagenetic apatite and late diagenetic ankerite-ferroan dolomite crystals constitute the remaining mineral phases.

4. Geochemical analyses show trace element depletions with the exception of Ba, As, Cr, Zn and Sr. Barium is particularly abundant in hematite (66 ppm) and magnetite (24 ppm). Arsenic is concentrated in siderite (62 ppm), Fe-talc (48 ppm) and ankerite-Fe dolomite (20 ppm). Chromium dominates in hematite (25 ppm), magnetite (20 ppm), siderite (16 ppm) and magnetite (~50 ppm), with minor amounts in Fe-talc (13 ppm). Zinc is most abundant in Fe-talc and siderite, showing average contents of 44 and 25 ppm,

respectively. Strontium occurs in hematite (22 ppm) and magnetite (10 ppm). The ability of these trace metals to partition into ferric oxyhydroxides indicates that they were most likely brought to the seafloor with the sedimenting ferrihydrite particles, and once buried, subjected to remobilization via Fe(III) reduction, with subsequent re-sorption onto, or incorporation into, ferrous-iron containing minerals.

5. The geochemistry of BIF and S macrobands is controlled by competing clastic and chemical sedimentation. The new REE + Y data presented for BIF macrobands implies a marine origin and no significant crustal and/or metamorphic overprinting for the samples studied. S macrobands, however, appear to be controlled by clastic and volcano-clastic contributions, as demonstrated by REE + Y signatures, high Al_2O_3 and positive correlations with TiO_2 and Zr. Hence, in agreement with the sedimentological evidence, the clastic input during sedimentation of the Dales Gorge Member must be recognized.

6. Our data supports a dominantly mafic provenance for the S macrobands, namely the Fortescue and Weeli Wolli basalts. The REE depletion showed by the S macrobands (and Mt. McRae shale) with respect to the Fortescue and Weeli Wolli basalts suggests submarine weathering of the basaltic rocks. Likewise, the high chemical index of alteration, ranging from 69 to 98, would indicate deep chemical weathering of the source area and suggest that the parent rocks must have been subaerially exposed some time during the deposition of the sediments. Indeed, geochemical trends between source rocks, mixed chemical–detrital and pure chemical sediments indicates that even in the detritus-free rocks the chemical components were likely derived from both hydrothermal exhalations and weathering solutions from terrestrial sources.

Although these conclusions are particularly valid for BIF of the Dales Gorge Member they carry important implications for the understanding of other BIF-bearing successions. Certainly, preliminary data shows similar geochemical trends in other BIFs where the concentration of certain elements seems to have been governed by a compositional change of the upper continental crust throughout much of the Precambrian.

Acknowledgments

References

Ahn, J.H., Buseck, P.R., 1990. Hematite nanospheres of colloidal origin from a Precambrian banded iron formation. Science 250, 111–113.

Alibert, C., McCulloch, M.T., 1993. Rare earth element and neodymium isotopic compositions of the banded iron-formations and associated shales from the Hamersley, Western Australia. Geochim. Cosmochim. Acta 57, 187–204.

Alowitz, M.J., Scherer, M.M., 2002. Kinetics of nitrate, nitrite, and Cr(VI) reduction by iron metal. Environ. Sci. Technol. 36, 299–306.

Amajor, L.C., 1987. Major and trace elements geochemistry of Albin and Touronian shales from the Southern Benue trough, Nigeria. J. Afr. Earth Sci. 6, 633–641.

Arndt, N., 1991. High Ni in Archean tholeiites. Tectonophysics 187, 411–419.

Arndt, N., Bruzak, G., Reischmann, T., 2001. The oldest continental and oceanic plateaus: geochemistry of basalts and komatiites of the Pilbara Craton, Australia. In: Ernst, R.E., Buchan, K.L. (Eds.), Mantle Plumes: Their Identification Through Time. Geological Society of America Special Paper 352. Geological Society of America.

Ayres, D.E., 1972. Genesis of iron-bearing minerals in banded iron formation mesobands in the Dales Gorge Member, Hamersley Group, Western Australia. Econ. Geol. 67, 1214–1233.

Barley, M.E., Kerrich, R., Reudavy, I., Xie, Q., 2000. Late Archaean Ti-rich, Al-depleted komatiites and komatiitic volcaniclastic rocks from the Murchison terrane in Western Australia. Australian J. Earth Sci. 47, 873–883.

Barley, M.E., Pickard, A.L., 1999. An extensive, crustally-derived, 3325–3310 Ma silicic volcanoplutonic suite in the eastern Pilbara Craton: evidence from the Kelley Belt, McPhee Dome, and Corunna Downs Batholith. Precambrian Res. 96, 41–62.

Barley, M.E., Pickard, A.L., Sylvester, P.J., 1997. Emplacement of a large igneous province as a possible cause of banded iron formation 2.45 billion years ago. Nature 385, 55–58.

Barrett, T.J., 1981. Chemistry and mineralogy of Jurassic bedded chert overlying ophiolites in the north Apennines, Italy. Chem. Geol. 34, 289–317.

Bau, M., Dulski, P., 1996. Distribution of yttrium and rare-earth elements in the Penge and Kuruman Iron-Formations, Transvaal Supergroup, South Africa. Precambrian Res. 79, 37–55.

Bau, M., Möller, P., 1993. Rare earth element systematics of the chemically precipitated component in Early Precambrian iron-formations and the evolution of the terrestrial atmosphere–hydrosphere–lithosphere system. Geochim. Cosmochim. Acta 57, 2239–2249.

Baur, M.E., Hayes, J.M., Studley, S.A., Walter, M.R., 1985. Millimeter-scale variations of stable isotope abundances in carbonates from banded iron-formations in the Hamersley Group of Western Australia. Econ. Geol. 80, 270–282.

Becker, R.H., Clayton, R.N., 1972. Carbon isotopic evidence for the origin of a banded iron-formation in Western Australia. Geochim. Cosmochim. Acta 36, 577–595.

Becker, R.H., Clayton, R.N., 1976. Oxygen isotope study of a precambrian banded iron formation, Hamersley Range, Western Australia. Geochim. Cosmochim. Acta 40, 1153–1165.

Benjamin, M.M., Leckie, J.O., 1981. Multiple site adsorption of Cd, Cu, Zn and Pb on amorphous iron oxy-hydroxides. J. Colloid Interface Sci. 79, 209–222.

Berry, J.A., Danyushevsky, L.V., O'Neill, H.St.C., Newville, M., Sutton, S.R., 2008. Oxidation state of iron in komatiitic melt inclusions indicates hot Archean mantle. Nature 455, 960–963.

Beukes, N.J., Klein, C., 1990. Geochemistry and sedimentology of a facies transition from microbanded to granular iron-formation in the early Proterozoic Transvaal Supergroup, South Africa. Precambrian Res. 47, 99–139.

Beukes, N.J., Klein, C., Kaufmann, A.J., Hayes, J.M., 1990. Carbonate petrography, kerogen distribution, and carbon and oxygen isotopic variations in an Early Proterozoic transition from limestone to iron-formation deposition, Transvaal Supergroup, South Africa. Econ. Geol. 85, 663–690.

Bickle, M.J., Bettenay, L.F., Chapman, H.J., Groves, D.I., McNaughton, N.J., Campbell, I.H., de Laeter, J.R., 1993. Origin of the 3500–3300 Ma calc-alkaline rocks in the Pilbara Archean: isotopic and geochemical evidence from the Shaw Batholith. Precambrian Res. 60, 117–149.

Bjerrum, C.J., Canfield, D.E., 2002. Ocean productivity before about 1.9 Gyr limited by phosphorous adsorption onto iron oxides. Nature 417, 159–162.

Bolhar, R., Kamber, B.S., Moorbath, S., Fedo, C.M., Whitehouse, M.J., 2004. Characterisation of early Archaean chemical sediments by trace element signatures. Earth Planet Sci. Lett. 222, 43–60.

Boström, K., 1973. The origin and fate of ferromanganoan active ridge sediments. Stockh. Contrib. Geol. 27, 149–243.

Braterman, P.S., Cairns-Smith, A.G., 1987. Photoprecipitation and the banded iron-formations-some quantitative aspects. Origin Life 17, 221–226.

Burdige, D.J., 2006. Geochemistry of Marine Sediments. Princeton University Press, Princeton/Oxford.

Burt, D.M., 1972. The system Fe-Si-C-O-H: a model for metamorphosed iron formations. In: Carnegie Institute Washington Year Book 1971–1972. Carnegie Institute, Washington.

Cairns-Smith, A.G., 1978. Precambrian solution photochemistry, inverse segregation, and banded iron formations. Nature 76, 807–808.

Canfield, D.E., 1998. A new model for Proterozoic ocean chemistry. Nature 396, 450–453.

Chen, J.M., Hao, O.J., 1996. Environmental factors and modeling in microbial chromium (VI) reduction. Water Environ. Res. 68, 1156–1164.

Chester, R., 2000. Marine Geochemistry, 2nd ed. Blackwell Science, Oxford.

Chown, E.H., N'dah, E., Mueller, W.U., 2000. The relation between iron-formation and low temperature hydrothermal alteration in an Archean volcanic environment. Precambrian Res. 101, 263–275.

Cloud Jr., P.E., 1965. Significance of the Gunflint (Precambrian) microflora. Science 148, 27–35.

Cloud, P.E., 1968. Atmospheric and hydrospheric evolution of the primitive earth. Science 160, 729–736.

Condie, K.C., 1993. Chemical composition and evolution of the upper continental crust: contrasting results from surface samples and shales. Chem. Geol. 104, 1–37.

Deer, W.A., Howie, R.A., Zussman, J., 1962. Rock Forming Minerals, vol. 3., 1st ed. Wiley, New York.

Dekov, V.M., Scholten, J.C., Botz, R., Garbe-Schönberg, C.D., Stoffers, P., 2007. Fe-Mn-(hydr)oxide-carbonate crusts from the Kebrit Deep, Red Sea: precipitation at the seawater/brine redoxcline. Marine Geol. 236, 95–119.

Deng, Y., Stjernström, M., Banwart, S., 1996. Accumulation and remobilization of aqueous chromium(VI) at iron oxide surfaces: application of a thin-film continuous flow-through reactor. J. Contam. Hydrol. 21, 141–151.

Derry, L.A., Jacobsen, S.B., 1990. The chemical evolution of Precambrian sea-water: evidence from REEs in banded iron formations. Geochim. Cosmochim. Acta 54, 2965–2977.

Drever, J.I., 1974. Geochemical model for the origin of Precambrian Banded Iron Formations. GSA Bull. 85, 1099–1106.

Dymek, R.F., Klein, C., 1988. Chemistry, petrology, and origin of banded iron formation lithologies from the 3800 Ma Isua Supracrustal Belt, West Greenland. Precambrian Res. 39, 247–302.

Dymond, J., Suess, E., Lyle, M., 1992. Barium in deep-sea sediment: a geochemical proxy for paleoproductivity. Paleoceanography 7, 163–181.

Ewers, W.E., Morris, R.C., 1981. Studies of the Dales Gorge Member of the Brockman Iron Formation, Western Australia. Econ. Geol. 76, 1929–1953.

Fedo, C.M., Eriksson, K., Krogstad, E.J., 1996. Geochemistry of shale from the Archean (~3.0 Ga) Buhwa Greenstone belt, Zimbabwe: implications for provenance and source area weathering. Geochim. Cosmochim. Acta 60, 1751–1763.

Fedo, C.M., Nesbitt, H.W., Young, G.M., 1995. Unravelling the effects of potassium metasomatism in sedimentary rocks and paleosols, with implications for paleoweathering conditions and provenance. Geology 23, 921–924.

Feely, R.A., Gendron, J.F., Baker, E.T., Lebon, G.T., 1994. Hydrothermal plumes along the East Pacific Rise, 8°40′ to 11°50′N: particle distribution and composition. Earth Planet. Sci. Lett. 128, 19–36.

Frey, F.A., Bryan, W.B., Thompson, G., 1974. Atlantic Ocean floor: geochemistry and petrology of basalts from legs 2 and 3 of the Deep-Sea Drilling Project. J. Geophys. Res. 79, 5507–5526.

Frost, C.D., von Blankenburg, F., Schoenberg, R., Frost, B.R., Swapp, S.M., 2007. Preservation of Fe isotope heterogeneities during diagenesis and metamorphism of banded iron formation. Contrib. Miner. Petrol. 153, 211–235.

Gibbs, A.K., Montgomery, C.W., O-Day, P.A., Erslev, E.A., 1986. The Archean–Proterozoic transition: evidence from the geochemistry of metasedimentary rocks of Guyana and Montana. Geochim. Cosmochim. Acta 50, 2125–2141.

Glasby, G.P., Schulz, H.D., 1999. Eh, pH diagrams for Mn, Fe, Co, Ni, Cu and As under seawater conditions: application of two new types of the Eh, pH diagrams to the study of specific problems in marine geochemistry. Aquatic Geochem. 5, 227–248.

Goldberg, E.D., Arrhenius, G.O.S., 1958. Chemistry of Pacific pelagic sediments. Geochim. Cosmochim. Acta 13, 153–212.

Gurvich, E.G., 2005. Metalliferous Sediments of the World Ocean: Fundamental Theory of Deep-Sea Hydrothermal Sedimentation. Springer, Berlin.

Hamade, T., Konhauser, K.O., Raiswell, R., Goldsmith, S., Morris, R.C., 2003. Using Ge/Si ratios to decouple iron and silica fluxes in Precambrian banded iron formations. Geology 31, 35–38.

Holland, H.D., 1984. The Chemical Evolution of the Atmosphere and Oceans. Princeton University Press, New Jersey.

Holland, H.D., 1999. When did the Earth's atmosphere become oxic? A reply. The Geochemical News 100, 20–22.

Holland, H.D., 2006. The oxygenation of the atmosphere and oceans. Philos. Trans. Soc. B 361, 903–916.

Isambert, A., Reynard, B., Gloter, A., Guyot, F., Valet, J.-P., 2005. Temperature and time dependent growth of magnetite derived from siderite decomposition: *in situ* Raman spectroscopy and magnetic susceptibility measurements. Geophys. Res. Abstr. 7.

Jacobsen, S.B., Pimentel-Klose, M.R., 1988. A Nd isotopic study of the Hamersley and Michipicoten banded iron formations: the source of REE and Fe in Archean oceans. Earth Planet. Sci. Lett. 87, 29–44.

James, H.L., 1988. Precambrian iron-formations: nature, origin, and mineralogic evolution from sedimentation to metamorphism. In: Wolf, K.H., Chilingarian, G.V. (Eds.), Diagenesis, III. Developments in Sedimentology, vol. 47. Elsevier, Amsterdam.

Jarosewich, E., 2002. Smithsonian microbeam standards. J. Res. Natl. Inst. Stand. Technol. 107, 681–685.

Johnson, C.M., Beard, B.L., Klein, C., Beukes, N.J., Roden, E.E., 2008. Iron isotopes constrain biologic and abiologic processes in Banded Iron Formation genesis. Geochim. Cosmochim. Acta 72, 151–169.

Kamber, B.S., Greig, A., Collerson, K.D., 2005. A new estimate for the composition of weathered young upper continental crust from alluvial sediments, Queensland, Australia. Geochim. Cosmochim. Acta 69, 1041–1058.

Kappler, A., Pasquero, C., Konhauser, K.O., Newman, D.K., 2005. Deposition of banded iron formations by anoxygenic phototrophic Fe(II)-oxidizing bacteria. GSA 33, 865–868.

Kaufman, A.J., 1996. Geochemical and mineralogic effects of contact metamorphism on banded iron-formation: an example from the Transvaal Basin, South Africa. Precambrian Res. 79, 171–194.

Kaufman, A.J., Hayes, J.M., Klein, C., 1990. Primary and diagenetic controls of isotopic compositions of iron-formation carbonates. Geochim. Cosmochim. Acta 54, 3461–3473.

Kendelewicz, T., Liu, P., Doyle, C.S., Brown G.E.Jr., 2000. Spectroscopic study of the reaction of aqueous Cr(VI) with Fe_3O_4 (1 1 1) surfaces. Surface Sci. 469, 144–163.

Klein, C., 1983. Diagenesis and metamorphism of Precambrian banded iron-formations. In: Trendall, A.F., Morris, R.C. (Eds.), Iron-formation: Facts and Problems. Elsevier, Amsterdam.

Klein, C., 2005. Some Precambrian banded iron-formations (BIFs) from around the world: their age, geologic setting, mineralogy, metamorphism, geochemistry, and origin. Am. Miner. 90, 1473–1499.

Klein, C., Beukes, N.J., 1989. Geochemistry and sedimentology of a facies transition from limestone to iron-formation deposition in the Early Proterozoic Transvaal Supergroup, South Africa. Econ. Geol. 84, 1733–1774.

Klein, C., Beukes, N.J., 1992. Time distribution, stratigraphy, and sedimentologic setting, and geochemistry of Precambrian iron formation. In: Schopf, J.W., Klein, C. (Eds.), The Proterozoic Biosphere: A Multidisciplinary Study. Cambridge University Press, New York.

Klein, C., Beukes, N.J., 1993. Sedimentology and geochemistry of the glaciogenic Late Proterozoic Rapitan Iron-Formation in Canada. Econ. Geol. 88, 542–565.

Klein, C., Gole, M.J., 1981. Mineralogy and petrology of parts of the Marra Mamba Iron Formation, Hamersley Basin, Western Australia. Am. Mineral. 66, 507–525.

Koziol, A.M., 1999. Experimental determination of siderite (iron carbonate) stability under moderate pressure-temperature conditions and application to martian carbonate parageneses. In: Lunar and Planetary Science XXX, Abstract #1226. Lunar and Planetary Institute, Houston (CD-ROM).

Konhauser, K.O., Hamade, T., Raiswell, R., Morris, R.C., Ferris, F.G., Southam, G., Canfield, D.E., 2002. Could bacteria have formed the Precambrian banded iron formations? Geology 30, 1079–1082.

Konhauser, K.O., Lalonde, S., Amskold, L., Holland, H.D., 2007a. Was there really an Archean phosphate crisis? Science 315, 1234.

Konhauser, K.O., Amskold, L., Lalonde, S.V., Posth, N.R., Kappler, A., Anbar, A., 2007b. Decoupling photochemical Fe(II) oxidation from shallow-water BIF deposition. Earth Planet. Sci. Lett. 258, 87–100.

Konhauser, K.O., Pecoits, E., Lalonde, S.V., Papineau, D., Nisbet, E.G., Barley, M.E., Arndt, N.T., Zahnle, K., Kamber, B.S., 2009. Oceanic nickel depletion and a methanogen famine before the great oxidation event. Nature 458, 750–753.

Krapež, B., Barley, M.E., Pickard, A.L., 2003. Hydrothermal and resedimented origins of the precursor sediments to banded iron-formation: sedimentological evidence from the Early Palaeoproterozoic Brockman Supersequence of Western Australia. Sedimentology 50, 979–1011.

Lascelles, D.F., 2007. Black smokers and density currents: a uniformitarian model for the genesis of banded iron-formations. Ore Geol. Rev. 32, 381–411.

Le Guern, C., Baranger, P., Crouzet, C., Bodenan, F., Conil, P., 2003. Arsenic trapping by iron oxyhydroxides and carbonates at hydrothermal spring outlets. Appl. Geochem. 18, 1313–1323.

Leleyter, L., Probst, J.-L., Depetris, P., Haida, S., Mortatti, J., Rouault, R., Samuel, J., 1999. REE distribution pattern in river sediments: partitioning into residual and labile fractions labile fractions. Comptes Rendus Geosci. 329, 45–52.

Lovley, D.R., 1993. Dissimilatory metal reduction. Annu. Rev. Microbiol. 47, 263–290.

Maliva, R.G., Knoll, A.H., Simonson, B.M., 2005. Secular change in the Precambrian silica cycle: insights from chert petrology. GSA Bull. 117, 835–845.

McConchie, D., 1987. The geology and geochemistry of the Joffre and Whaleback Shale members of the Brockman Iron Formation, Western Australia. In: Appel, P.W.U., LaBerge, G.L. (Eds.), Precambrian Iron-Formations. Theophrastus, Athens.

McLennan, S.M., Hemming, S., McDaniel, D.K., Hanson, G.N., 1993. Geochemical approaches to sedimentation, provenance, and tectonics. In: Johnson, M.J., Basu, A. (Eds.), Processes Controlling the Composition of Clastic Sediments. GSA Special Paper 284. GSA, Boulder, Colorado.

McLennan, S.M., Taylor, S.R., 1991. Sedimentary rocks and crustal evolution: tectonic setting and secular trends. J. Geol. 99, 1–21.

McLennan, S.M., Taylor, S.R., Eriksson, K.A., 1983. Geochemistry of Archean shales from Pilbara Supergroup, Western Australia. Geochim. Cosmochim. Acta 47, 1211–1222.

Miller, R.G., O'Nions, R.K., 1985. Source of Precambrian, chemical and clastic sediments. Nature 314, 325–330.

Millero, F.J., 1996. Chemical Oceanography, 2nd ed. CRC-Press, Boca Raton.

Morris, R.C., 1993. Genetic modeling for banded iron-formations of the Hamersley Group, Pilbara Craton, Western Australia. Precambrian Res. 60, 243–286.

Mueller, W.U., Stix, J., Corcoran, P.L., Daigneault, R., 2009. Subaqueous calderas in the Archean Abitibi greenstone belt: an overview and new ideas. Ore Geol. Rev. 35, 4–46.

Nelson, D.R., Trendall, A.F., de Laeter, J.R., Grobler, N.J., Fletcher, I.R., 1992. A comparative study of the geochemical and isotopic systematics of late Archaean flood basalts from the Pilbara and Kaapvaal Cratons. Precambrian Res. 54, 231–256.

Nesbitt, H.W., 1979. Mobility and fractionation of rare earth elements during weathering of a granodiorite. Nature 279, 206–210.

Nesbitt, R.W., Sun, S.-S., Purvis, A.C., 1979. Komatiites: geochemistry and genesis. Can. Miner. 17, 165–186.

Nesbitt, H.W., Young, G.M., 1982. Early Proterozoic climates and plate motions inferred from major element chemistry of lutites. Nature 199, 715–717.

Nesbitt, H.W., Young, G.M., 1989. Formation and diagenesis of weathering profiles. J. Geol. 97, 129–147.

Nisbet, E.G., Arndt, N.T., Bickle, M.J., Cameron, W.E., Chauvel, C., Cheadle, M., Hegner, E., Kyser, T.K., Martin, A., Renner, R., Roedder, E., 1987. Uniquely fresh 2.7 Ga komatiites from the Belingwe greenstone belt, Zimbabwe. Geology 15, 1147–1150.

Ohta, H., Maruyama, S., Takahashi, E., Watanabe, Y., Kato, Y., 1996. Field occurrence, geochemistry and petrogenesis of the Archaean Mid-Oceanic Ridge Basalts (A-MORBs) of the Cleaverville area, Pilbara Craton, Western Australia. Lithos 37, 199–221.

Ohmoto, H., 2003. Nonredox transformations of magnetite–hematite in hydrothermal systems. Econ. Geol. 98, 157–161.

Ohmoto, H., Watanabe, Y., Yamaguchi, K.E., Naraoka, H., Haruna, M., Kakegawa, T., Hayashi, K., Kato, Y., 2006. Chemical and biological evolution of early Earth: constraints from banded iron formations. In: Kesler, S.E., Ohmoto, H. (Eds.), Evolution of Early Earth's Atmosphere, Hydrosphere, and Biosphere-Constraints from Ore Deposits, vol. 198. GSA Memoir, pp. 291–331.

Partridge, M.A., Golding, S.D., Baublys, K.A., Young, E., 2008. Pyrite paragenesis and multiple sulfur isotope distribution in late Archean and early

Paleoproterozoic Hamersley Basin sediments. Earth Planet. Sci. Lett. 272, 41–49.

Perry Jr., E.C., Tan, F.C., Morey, G.B., 1973. Geology and stable isotope geochemistry of the Biwabiki Iron Formation, northern Minnesota. Econ. Geol. 68, 1110–1125.

Pickard, A.L., 2002. SHRIMP U–Pb zircon ages of tuffaceous mudrocks in the Brockman Iron Formation of the Hamersley Range, Western Australia. Austr. J. Earth Sci. 49, 3491–3507.

Pickard, A.L., 2003. Genetic stratigraphy and composition of the Dales Gorge Member, Brockman Iron Formation in Western Australia, and the correlation of the Paleoproterozoic Brockman and Kuruman iron formations using high-precision geochemistry and U–Pb SHRIMP geochronology. Ph.D. Thesis. University of Western Australia (unpublished).

Pickard, A.L., Barley, M.E., Krapež, B., 2004. Deep-marine depositional setting of banded iron formation: sedimentological evidence from interbedded clastic sedimentary rocks in the early Paleoproterozoic Dales Gorge Member of Western Australia. Sedimentary Geol. 170, 37–62.

Posth, N.R., Hegler, F., Konhauser, K.O., Kappler, A., 2008. Alternating Si and Fe deposition caused by temperature fluctuations in Precambrian oceans. Nat. Geosci. 1, 703–708.

Romanek, C.S., Zhang, C.L., Li, Y., Horita, J., Cole, D.R., Vali, H., 2003. Carbon and hydrogen isotope fractionations associated with dissimilatory iron-reducing bacteria. Chem. Geol. 195, 5–16.

Ruhlin, D.E., Owen, R.M., 1986. The rare earth element geochemistry of hydrothermal sediments from the East Pacific Rise; examination of a seawater scavenging mechanism. Geochim. Cosmochim. Acta 50, 393–400.

Rye, R., Holland, H.D., 2000. Geology and geochemistry of paleosols developed on the Hekpoort basalt, Pretoria Group, South Africa. Am. J. Sci. 300, 85–141.

Saito, M.A., Sigman, M.D., Morel, F.M.M., 2003. The bioinorganic chemistry of the ancient ocean: the co-evolution of cyanobacterial metal requirements and biogeochemical cycles at the Archean-Proterozoic boundary? Inorg. Chim. Acta 356, 308–318.

Schwertmann, U., Murad, E., 1983. Effect of pH on the formation of goethite and hematite from ferrihydrite. Clays Clay Miner. 31, 277–284.

Smith, R.E., Perdix, J.L., Parks, T.C., 1982. Burial metamorphism in the Hamersley Basin, Western Australia. J. Petrol. 23, 75–102.

Smithies, R.H., Van Kranendonk, M.J., Champion, D.C., 2007. The Mesoarchean emergence of modern style subduction. Gondwana Res. 11, 50–68.

Swedlund, P.J., Webster, J.G., 1999. Adsorption and polymerization of silicic acid on ferrihydrite, and its effect on arsenic adsorption. Water Res. 33, 3413–3422.

Taylor, St.R., McLennan, S.M., 1985. The Continental Crust: Its Composition and Evolution. Blackwell, Oxford.

Trendall, A.F., 2002. The significance of iron-formation in the Precambrian stratigraphic record. In: Altermann, W., Corcorane, P.L. (Eds.), Precambrian Sedimentary Environments: A Modern Approach to Depositional Systems. IAS Special Publication 44. Blackwell Science, Oxford.

Trendall, A.F., 1983. Introduction. In: Trendall, A.F., Morris, R.C. (Eds.), Iron Formation: Facts and Problems. Elsevier, Amsterdam.

Trendall, A.F., Blockley, J.G., 1970. The iron-formations of the Precambrian Hamersley Group, Western Australia. Geol. Surv. West. Aust. Bull., 119.

Trendall, A.F., Compston, W., Nelson, D.R., De Laeter, J.R., Bennett, V.C., 2004. SHRIMP zircon ages constraining the depositional chronology of the Hamersley Group, Western Australia. Aust. J. Earth Sci. 51, 621–644.

Trendall, A.F., Pepper, R.S., 1977. Chemical composition of the Brockman Iron Formation. Geol. Surv. West. Aust. Record No. 1976/25.

Trivedi, P., Axe, L., 1999. A comparison of strontium sorption to hydrous aluminum, iron, and manganese oxides. J. Colloid Interface Sci. 218, 554–563.

Turekian, K.K., Tausch, E.H., 1964. Barium in deep-sea sediments of the Atlantic Ocean. Nature 201, 696–697.

Walker, J.C., 1984. Suboxic diagenesis in banded iron formations. Nature 309, 340–342.

Webb, A.D., Dickens, G.R., Oliver, N.H.S., 2003. From banded iron-formation to iron ore: geochemical and mineralogical constraints from across the Hamersley Province, Western Australia. Chem. Geol. 197, 215–251.

White, A.F., Peterson, M.L., 1996. Reduction of aqueous transition metal species on the surfaces of Fe(II)-containing oxides. Geochim. Cosmochim. Acta 60, 3799–3814.

Widdel, F., Schnell, S., Heising, S., Ehrenreich, A., Assmus, B., Schink, B., 1993. Ferrous iron oxidation by anoxygenic phototrophic bacteria. Nature 362, 834–836.

Zachara, J.M., Kittrick, J.A., Harsh, J.B., 1988. The mechanism of Zn^{2+} adsorption on calcite. Geochim. Cosmochim. Acta 52, 2281–2291.